

UNIVERSITY OF TWENTE

BACHELOR THESIS

3D Printed Flexible Fingertip Strain Sensor

Author:

Eddo HOBERT

Supervisor:

prof. dr. ir. G.J.M. KRIJNEN

Committee:

prof. dr. ir. G.J.M. KRIJNEN

dr. ir. R.A.R. VAN DER ZEE

ing. R.G.P. SANDERS

ELECTRICAL ENGINEERING
ROBOTICS AND MECHATRONICS

June 30, 2017

Abstract

Tactile sensing helps humans in determining properties of objects that we touch, like texture. Recent techniques allow a combination of conductive and nonconductive thermoplastic polyurethane (TPU) to be 3D-printed. This enables the possibility to 3D-print flexible tactile sensors that can be used on the fingertips of humans or robots. This is advantageous, because flexible sensors can better adapt to the shape of a fingertip than the more traditional metallic sensors. This report describes the modelling, designing and characterization of a 3D-printed flexible fingertip strain sensor. This sensor can measure static and dynamic normal forces acting on a fingertip. A study on the material properties of TPU was conducted prior to constructing a model. This study yielded results on the Young's modulus and resistivity of the conductive TPU that deviate significantly from the specifications given in the datasheet provided by the manufacturer. The results following from this study were used in the construction of a first mathematical model of the sensor. Based on the model, a novel foldable sensor design was introduced. The design comprises a force sensitive resistor (FSR) that can be strapped around a finger and fastened with a rod and a belt. 12 versions of the design with different dimensions were 3D-printed. Measurements on these sensors show resistances in the order of megaohms. The measurements indicate that the sensors with smaller heights and larger lengths and widths yield more sensitive responses for smaller forces. Hysteresis was found to have a significant impact on the resistance measurements. The model accurately predicted whether a sensor made contact in 10 out of 12 sensors, but only in some cases did the model predict a resistance/force relation that looked similar in shape to the measurements. The model gives qualitative insight in the sensor's physical operation, but requires significant optimizations to make more accurate predictions and give a better understanding of the sensor. Other difficulties that are yet to be overcome in this field of research are printing limitations on sensors with small sizes, finding an optimal transduction principle and improving on the design of 3D-printed tactile sensors.

Contents

1	Introduction	1
1.1	Tactile sensing	1
1.2	3D-Printing a Flexible Sensor	1
1.3	Research Goals	2
1.4	Thesis Outline	2
2	Types of Sensors	3
2.1	Introduction	3
2.2	Overview	3
2.3	Discussion	4
2.4	Conclusion	4
3	Material Properties of NinjaFlex and PI-ETPU	5
3.1	Introduction	5
3.2	Young's Modulus and Poisson's Ratio	5
3.3	Resistivity and Surface Resistance	14
3.4	Discussion	19
3.5	Conclusion	21
4	Sensor Modelling and Design	22
4.1	Introduction	22
4.2	Model	22
4.3	Design	25
4.4	Discussion	27
4.5	Conclusion	28
5	Sensor Characterization	29
5.1	Introduction	29
5.2	Method	29
5.3	Measurements	31
5.4	Discussion	35
5.5	Conclusion	38
6	Conclusion and Recommendations	39
6.1	Conclusion	39
6.2	Recommendations	40
A	Tables	41

B Graphs	42
B.1 Young's Modulus	42
B.2 Sensor Modelling and Design	46
B.3 Sensor Characterization	47
C Equations	52
Bibliography	53

1 Introduction

1.1 Tactile sensing

Human sensory perception consists of an extensive combination and integration of different sensors that establish the way in which we perceive the world around us. A part of this perception consists of tactile sensing. Tactile sensing helps humans in determining properties of the objects that we touch, like texture and temperature. This enables us to appropriately adapt the way we handle these objects. For example, with the help of tactile sensory input, we adjust the force we apply to an object or the distance we keep from an object.

Strain sensors made for human fingertips allow us to analyse the forces acting on our hands and fingers. Given the flexibility of the human skin, it would be preferable to have tactile force sensors that are flexible as well. This way a sensor can dynamically follow the shape of the fingertip that it is attached to. In case of robotics, fingertip force sensors could be useful in case some robotic gripper would have to handle objects of varying dimensions or objects that are fragile, for example. Force sensor feedback could then allow a robot to apply a suitable amount of force to an object. Having flexible force sensors thus is advantageous, because they can adapt to the shape of a fingertip and they could be more robust than non-flexible sensors (3; 7; 9; 24; 26; 28).

1.2 3D-Printing a Flexible Sensor

A significant amount of research has already been conducted on (partly) flexible force sensors for usage on fingertips of humans and robots. A variety of fabrication processes and transduction techniques have been introduced in these researches. An example is a research by Drimus et al. (9), in which the design and realization of a fingertip force sensor that measures both the location and magnitude of an applied force is introduced. In this case, the sensor is not fully flexible as it holds metal components. In a paper by Hammond et al. (11), a flexible force sensor that can measure forces on the distal, middle and proximal phalanges (i.e. the top, middle and bottom finger segments, respectively) based on the deformation of liquid-metal channels is described. The sensor is created by means of moulding and assembling different parts. Büscher et al. (3) discusses the designing and making of a tactile force sensing glove made from fabrics. In Chorley et al. (4) the design of an optical finger-inspired sensor is described. This is a large sensor meant for robotics and forces up to 0.05N. Vatani et al. (28) describes a multi-layer piezoresistive tactile force sensor that was fabricated using hybrid 3D printing with soft moulding, conformal direct-print and photocuring processes. The sensor is meant to detect the position of applied forces. Most of the already conducted research on flexible force sensors is on sensors that are not fully flexible, require different fabrication processes and/or include an (extensive) assembly. Additive manufacturing (3D-printing) has the potential to simplify and speed up the fabrication process of such tactile force sensors.

Multi-material additive manufacturing of thermoplastic polyurethane (TPU) allows for the creation of flexible structures that consist of a combination of conductive and nonconductive segments. This enables the possibility to fabricate fully flexible strain sensors. Additive manufacturing of TPU is generally done in a process called fused deposition modelling. In this process the TPU becomes fluidic under the application of heat. In its fluidic form the TPU is added layer-upon-layer via an extruder that follows a certain pattern to form a specified structure. Hereafter, the structure solidifies when cooled (1). Figure 1.1 shows a graphical representation of the process of fused deposition modelling where (1) represents the printer

extruder, (2) is the layer-by-layer structure being printed and (3) is a heated bed to keep the layers from cooling down too rapidly as this could adversely affect the layer-to-layer adhesion.

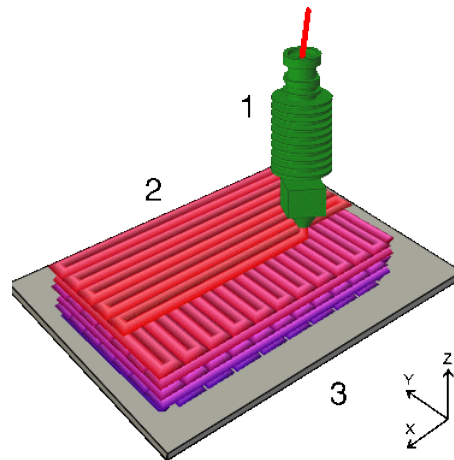


Figure 1.1: Graphical representation of fused deposit modeling (19)

1.3 Research Goals

Specific material properties of thermoplastic polyurethane need to be determined by means of researching and testing. This should help in determining what types of sensors can be 3D-printed and used to measure forces. The sensor is to be placed on a fingertip, so it should be as small as possible. As the potential benefit of 3D-printing a tactile sensor is mainly apparent in the speed and simplicity of production, the sensor should be producible with a single print after which no further assembly should be required. It should be analysed how such a strain sensor could achieve normal (1-DOF) and, if time permits, shear force measurements (3-DOF). Of the most effective or promising type of sensor a design will be made, modelled and 3D-printed. Sensor performance will be characterized by a combination of electro- and mechanical tests. The just mentioned research goals and subgoals are summarized in a list below:

- Find and analyse TPU material properties that will have an influence on sensor performance and use this information in the design.
- Design and make a strain sensor that can measure the normal force acting on a fingertip.
 - The design should be novel and based on the most suitable transduction principle.
 - The sensor should be as small as possible.
 - Producing the sensor should be possible in a single 3D print.
 - Besides connecting wires, the sensor should require no further assembly.
- Characterize sensor performance.
- If time permits, it should be researched if and how shear forces could be measured as well.

1.4 Thesis Outline

This report consists of 6 chapters. Chapter 1 presents a general introduction to the report. In chapter 2, different possible transduction principles for fingertip force sensors are analysed. The material properties of TPU that are significant in designing the sensor are analysed in chapter 3. Chapter 4 elaborates on the modelling and designing of the sensor. Characterization of the sensor is discussed in chapter 5. Finally, chapter 6 comprises the conclusion on the research and recommendations for further research on this topic.

2 Types of Sensors

2.1 Introduction

A goal of this research is to design and make a fingertip force sensor. There are multiple transduction principles with which this goal could be achieved. Given that the sensor will be 3D-printed from flexible TPU and placed on fingertips of humans or robots, some transduction techniques are likely to perform better than others. There is limited time available to conduct this research, so it is preferable to utilize a transduction technique that is easy to conduct measurements on. Furthermore, one of the subgoals is that the sensor should eventually have a novel design. In the remainder of this chapter an analysis of the transduction principle most suitable for 3D-printed flexible fingertip force sensors is presented.

2.2 Overview

Reviews on the most commonly used transduction principles have been conducted in Dahiya et al. (7); Dahiya and Valle (8); R.M. Crowder (23); Tiwana et al. (26); Wei and Xu (30). A summarized general overview of these reviews is given in table 2.1.

Table 2.1: List of advantages and disadvantages of common transduction principles used in force sensors

Transduction principle	Advantages	Disadvantages
Capacitive	<ul style="list-style-type: none"> • Excellent sensitivity • Good spatial resolution • Large dynamic range 	<ul style="list-style-type: none"> • Hysteresis • Noise susceptible • Stray capacitance • Complex electronics
Piezoelectric	<ul style="list-style-type: none"> • High sensitivity • Large dynamic range • High frequency response 	<ul style="list-style-type: none"> • Temperature sensitive • No static sensing • High stiffness • Special materials/fabrication required
Resistive (Piezoresistive strain gauge, FSR)	<ul style="list-style-type: none"> • High sensitivity • Sensing range • Low noise • Simple electronics • Low cost 	<ul style="list-style-type: none"> • Hysteresis • Temperature and humidity sensitive • Non-linearity • High power consumption • Intensive manufacturing process

Other common transduction principles like optical and magnetic type of force sensors have been omitted from this overview. This is because they are not feasible and/or would take too much time given the limited available time for this research and given the limitations on sensor complexity imposed by 3D-printing.

2.3 Discussion

Table 2.1 shows that all four transduction principles have a high sensitivity. Capacitive type of sensors suffer from hysteresis, noise, stray capacitance and require complex electronics for measurements. These all contribute to making the measurements more difficult. Moreover, the presence of a human fingertip will probably affect the capacitance differently than the presence of a robotic fingertip. Piezoelectric type of sensors do not suffer from hysteresis like capacitive types do, but they are temperature sensitive and do not measure static forces. Also, they have a high stiffness and that would be nonideal on human fingertips, which have a somewhat flexible nature. Resistive type sensors are also temperature sensitive and like capacitive types, they too suffer from hysteresis. Additionally, they are non-linear, consume more power and require an intensive manufacturing process. However, they do have low noise and simple electronics to compensate for the measurement difficulties. Based on table 2.1 no clear winner emerges. All transduction principles have some serious advantages and disadvantages to go for them.

Now these were general advantages and disadvantages of sensors using these transduction principles. It was not taken into account that 3D-printed flexible TPU will be used to make a sensor. TPU is not a piezoelectric material by itself and as piezoelectric flexible 3D-printable material is not readily available, this type of sensor is not a feasible option. A capacitive sensor, strain gauge or FSR could be 3D-printed with the available TPU. As capacitive sensors generally require complex measurement electronics and resistive type of sensors do not, a resistive type of sensor will be focused on in this research. A strain gauge would ideally experience large deflections for better performance. However, one of the goals is to make the sensor as small as possible. Creating a 3D-printed strain gauge to measure the normal force acting on a fingertip would likely require a structure with a height that, when put on, would noticeably extend the length of a fingertip. A sensor that significantly extends the length of a fingertip is not preferable. The force sensitive resistor (FSR) is considered to be a sensor that experiences a change in resistance due to a change in contact area induced by an external force. (12) provides the theory of operation of a commercial FSR. An FSR could be realized by placing two plates on top of each other with some space in between. It is expected that it is easier to make the height of these plates and the gap in between smaller than it is to make a good performing strain gauge with a small height. Therefore, an FSR will be designed in this research. Hysteresis, temperature and humidity sensitivity, non-linearity and high power consumption will be a challenge to deal with. Another disadvantages listed for resistive sensors was the intensive manufacturing process that is traditionally required to produce a resistive sensor. One of the subgoals of this research is to make a sensor out of a single print that does not require an assembly, which would be the opposite of having an intensive manufacturing process. This makes the FSR a good option to work on during this research.

2.4 Conclusion

This chapter gave a summarized overview of advantages and disadvantages of three common transduction principles behind force sensors. From this overview it did not become clear which transduction principle would perform best. They all have some serious disadvantages and advantages to go for. When considering that the sensor will have to be 3D-printed, some transduction principles seem more feasible than others. TPU is not piezoelectric itself and a capacitive or resistive sensor can be made with the available TPU, so keeping in mind the limited available time for this research, piezoelectric transduction was deemed unfeasible. Resistive transduction was chosen over capacitive transduction, because of the expected electronic complexity of measuring a capacitive sensor. An FSR will be focused on in this research rather than a strain gauge, because it is expected that an FSR can be made smaller.

3 Material Properties of NinjaFlex and PI-ETPU

3.1 Introduction

The sensor will be constructed from conductive and nonconductive elastic thermoplastic polyurethane (TPU). The conductive and nonconductive TPU that are available and will be used are PI-ETPU 95-250 Carbon Black and NinjaFlex (Lava colour), respectively. In order to be able to accurately model and design a sensor, it is necessary to know the material specific properties that will influence sensor behaviour. The sensor will be flexible and thus elastic properties like the Young's modulus and Poisson's ratio are of interest. Also, as the sensor's electrical resistance will be measured as a function of contact area, its resistivity and surface resistance should be known. Properties like the Young's modulus and volume resistivity are given by the TPU manufacturers in the datasheets of the TPU filament (18; 20). However, these may not be accurate; the properties depend on various factors, like printing configuration, testing conditions and environmental conditions. It is because of such dependencies that the mentioned properties will be redetermined by means of research and electromechanical measurements.

This chapter is divided into two sections. Section 3.2 is devoted to the Young's modulus and the Poisson's ratio of NinjaFlex and PI-ETPU and section 3.3 is on the resistivity of PI-ETPU. In section 3.2 first some theory on the Young's modulus and Poisson's ratio is given, after which the methods used during the measurements are discussed. This is followed by a section on modelling and a section on designing. These follow after the method section, because the model and design are dependent on the measurement method. At the end of this section, the measurements are shown. The section on resistivity starts off with a brief explanation on the theory and methods that will be used. Then the designs of the structures used for doing resistance measurements with are discussed. This is followed by the measurement results. At the end of this chapter, a discussion on the Young's modulus measurements and resistivity measurements is given. The chapter is completed with a general conclusion.

3.2 Young's Modulus and Poisson's Ratio

3.2.1 Theory

The Young's modulus or tensile modulus is a measure of stiffness of an elastic material. It is used to describe the elastic properties of objects when they are stretched or compressed (The Engineering ToolBox). The Young's modulus for both NinjaFlex and PI-ETPU as given by their manufacturers is 12 MPa (18; 20). 3D-printed structures are generally anisotropic, which is the case when the properties of a material vary along different directions (NDT Resource Center). This can intuitively be seen in figure 1.1, where the layer-by-layer build-up of a structure make it anisotropic. This means that the Young's modulus of a structure can vary depending on the conditions under which it is used and the setting in effect during printing.

Equation 3.1 shows a mathematical description of the Young's modulus (E) according to Hooke's law, where σ and ε stand for stress and strain, respectively.

$$E = \frac{\sigma}{\varepsilon} \quad (3.1)$$

Thus, to be able to determine the Young's modulus, the present stress and strain should be known. Stress equals a force, F , divided by the area this force is being applied to, A . This area is determined by its width, w , times its height, h . Strain is a measure of relative deformation and is given by the change in length, ΔL , divided by the original length, L_0 . Equations 3.2 and 3.3 for stress and strain are given below (15).

$$\sigma = \frac{F}{A} = \frac{F}{w \cdot h} \quad (3.2)$$

$$\varepsilon = \frac{\Delta L}{L_0} \quad (3.3)$$

From equations 3.1, 3.2 and 3.3, equation 3.4 is derived.

$$E = \frac{F \cdot L_0}{w \cdot h \cdot \Delta L} \quad (3.4)$$

A graphical representation of the dimensions and force present in equation 3.4 is given in figure 3.1.

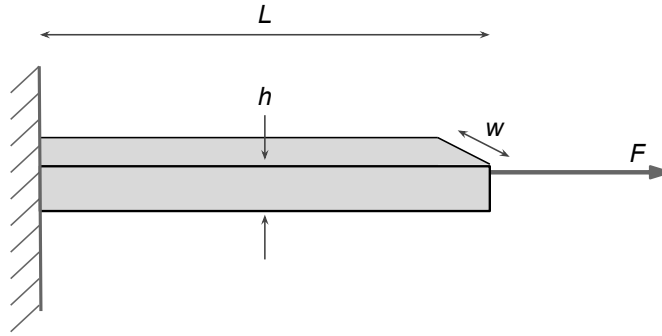


Figure 3.1: Beam stretching parameters needed for determining the Young's modulus

In figure 3.1, the length of the beam, L , equals its original length plus its elongation due to force F , i.e. $L = L_0 + \Delta L$. Due to the Poisson effect, the width and height of a material could change (decrease) when the material is elongated. This would result in a change in area, which would affect the stress and the Young's modulus. The change in width and length that accompany an elongation can be estimated if the Poisson's ratio, which has a specific value per material, is known. These changes are described by equations 3.5 and 3.6 below, where Δw and Δh are the changes in width and height and w_0 and h_0 are the original width and height, respectively (15). The Poisson's ratio is represented by ν .

$$\Delta w = -\nu \cdot w_0 \cdot \varepsilon = -\nu \cdot w_0 \cdot \frac{\Delta L}{L_0} \quad (3.5)$$

$$\Delta h = -\nu \cdot h_0 \cdot \varepsilon = -\nu \cdot h_0 \cdot \frac{\Delta L}{L_0} \quad (3.6)$$

The width and height at any moment are described by $w = w_0 + \Delta w$ and $h = h_0 + \Delta h$, respectively. Filling this in in equation 3.4, together with equations 3.5 and 3.6, yields equation 3.7.

$$\begin{aligned}
E &= \frac{F \cdot L_0}{(w_0 + \Delta w) \cdot (h_0 + \Delta h) \cdot \Delta L} \\
&= \frac{F \cdot L_0}{\left(w_0 - v \cdot w_0 \cdot \frac{\Delta L}{L_0}\right) \cdot \left(h_0 - v \cdot h_0 \cdot \frac{\Delta L}{L_0}\right) \cdot \Delta L} \\
&= \frac{F \cdot L_0}{w_0 \cdot h_0 \cdot \left(1 - v \cdot \frac{\Delta L}{L_0}\right)^2 \cdot \Delta L} \tag{3.7}
\end{aligned}$$

3.2.2 Method

Because the Young's modulus can vary depending on the conditions and printing settings during printing, multiple structures with different specifications were printed to be tested and evaluated with respect to how the Young's modulus varies among these structures. A straightforward way to determine the Young's modulus of TPU consists of using a measurement setup with which the variables in equation 3.7 can be measured directly. Except from the changes in width and height, such a setup was constructed in practise. In this setup a beam of TPU is clamped on both of its sides. One clamped side is attached to a fixed rigid structure and the other is attached to a freely moving load cell, which's purpose is to measure the force acting on the TPU. The load cell is attached via a sliding structure to a voice coil which is used to apply a force. Furthermore, a displacement sensor is attached to the sliding structure. This sensor measures the change in length of the TPU beam. Some details on the voice coil, load cell and displacement sensor are listed below.

- Load cell

The load cell being used is a calibrated TedeA-Huntleigh model 1022. Four-terminal sensing is applied to measure the voltage over the load cell, V_{out} . The force, F , acting on the load cell is calculated with equation 3.8.

$$F = -\frac{V_{out} \cdot E_{max}}{V_{ex} \cdot RO} \cdot g \tag{3.8}$$

Herein, E_{max} is the rated capacity of the load cell, which is 3 kg in this case. V_{ex} represents the recommended excitation voltage, which is 10 V (29). RO is the rated output of the load cell and equals 1.8342 mV/V according to the load test data sheet that is provided with the load cell. This datasheet was specifically established by the manufacturer for this particular unit. Finally, g represents Earth's gravitational acceleration of $\approx 9.81 \text{ m/s}^2$ (National Institute of Standards and Technology) and is included to convert the unit of force from kilogram to newton.

- Voice coil

The voice coil in use is an MB Electronics PM50. According to its datasheet, this voice coil has a rated peak output force of 25 pounds or approximately 11.3 kilograms for natural convection cooling and a peak to peak displacement of 0.5 inch or 12.7 millimetre (14). A fixed current ranging from 0 to 4 amperes is delivered to the voice coil. There is no linear relation between the current flowing through the voice coil (input) and the force or displacement outputted by the voice coil. Instead, the resulting displacement and force are established by an equilibrium being reached in the entire measurement setup. This equilibrium mainly depends on the structure being tested. For example, imagine two structures of the same material and with the same width and height, but with different lengths being tested. If for both structures the same current is delivered to the voice coil, then this will result in two different forces and displacements, due to two different equilibriums being reached.

- Displacement sensor

A digital displacement sensor reads the distance between the sliding structure and the fixed rigid structure with a resolution of 100 nm.

The current to the voice coil is delivered in steps of 0.1 ampere between 0 and 4 amperes. For each step, 50 force/displacement data points are collected with an added delay of 450 milliseconds between each of them. Also, each collected data point takes up about 50 milliseconds of processing time. Thus, each step takes about $50 \times (0.450 + 0.050) = 25$ seconds. In total, there are 41 steps, resulting in a total measurement duration of about $25 \times 41 = 1025$ seconds or approximately 17 minutes. The 450 milliseconds added delay serves two purposes. Firstly, it gives the measurement setup and structure being tested time to reach an equilibrium position. Secondly, the displacement sensor is unable to pass through data continuously without delay. When data from the displacement sensor is collected too quickly, its output value clips. The delay prevents this unwanted clipping behaviour.

As mentioned, the measurement setup does not measure the changes in width and height of a structure under testing. Thus, the Poisson's ratio is not measured. A Poisson's ratio of 0.5 is estimated for polyurethane (PU) in Tsukinovsky, D. et al. (27) and in Qi and Boyce (22) it is stated that for TPU "it is reasonable to assume the Poisson's ratio ranges from 0.48 to 0.5". In Elleuch et al. (10) a Poisson's ratio of 0.45 is assumed for TPU. Based on this information, an approximate average Poisson's ratio of 0.48 was assumed for both PI-ETPU and NinjaFlex throughout this research.

3.2.3 Beam Model

Beams with a length of 5 cm, height of 5 mm and varying width (thickness) were modelled in Matlab. This length and height had been chosen, because physical beams with these dimensions can be comfortably placed in the measurement setup. The measurement setup allows for easy clamping of beams with various thicknesses in the range of 0 to approximately 5 mm, so this dimension was chosen as a variable. The model is based on equation 3.7. Now only the force and the elongation are unknown, so either the force or the elongation needs to be driven in the model. A quick check with the measurement setup showed that the voice coil will output a displacement of about 2 mm for structures that will be tested. Therefore, in the model, the displacement (ΔL) was assumed to be driven and ranging from 0 to 2 mm, resulting in an according force (F). This is shown in figure 3.2.

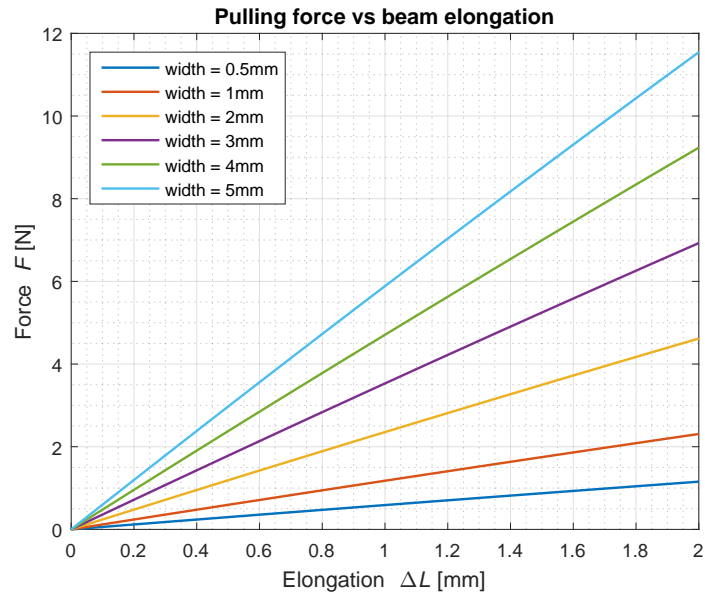


Figure 3.2: Modeled force vs elongation of beams with various thicknesses and with length = 5 cm and width = 5 mm

In the previous section it was mentioned that the voice coil should be able to deliver 11.3 kg (≈ 110.8 N) of force. Figure 3.2 indicates that the voice coil should be capable to deliver the modeled forces associated with the displacements. Additionally, figure B.1 shows a stress versus strain plot for various thicknesses. A single linear slope is visible, because the stress and strain are equal for all beams. This is because the Young's modulus is modelled as being the same for all.

3.2.4 Beam Design

A simple design was made for structures of NinjaFlex and PI-ETPU to be tested in the measurement setup. A cross-sectional view of this design is shown in figure 3.3.

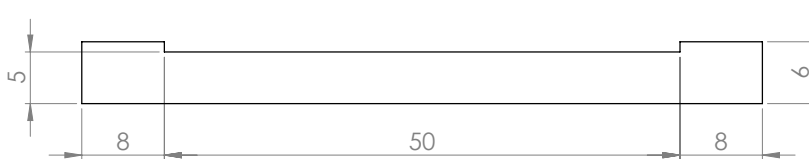


Figure 3.3: Cross-sectional view and dimensions [mm] of the structure to be tested in the measurement setup

The design consists of a 50 mm beam, with clamping pads on either side. The pads have a slightly larger height than the beam (6 mm vs 5 mm), so that in practise it can be easily seen if a length of 50 mm of material is being clamped without having to use a ruler. The thickness (width) is not shown in figure 3.3, but is equal throughout the design.

Figure 1.1 gives intuitive insight into what orientations the design could be printed in. There are two possible printing orientations in which no bridging or overhanging of TPU is required. The most straightforward method will be referred to as horizontal printing. Consider that the length of the design in figure 3.3 is oriented along the x-axis in figure 1.1 and the height of the design is oriented along the y-axis. Then the width is along the z-axis. This is horizontal

printing. Another possible method is when again the length is along the x-axis, but now the width is along the y-axis and the height is in the z-direction. This will be referred to as vertical printing. Other printing orientations are possible, but would require bridging or overhanging of material. This would be difficult to print accurately with the available material.

So which variations in beam thickness were designed? Thinner beams are easier to be clamped in the measurement setup, but beams with a thickness of less than 1 mm are difficult to print vertically due to the printer's limitation on resolution. In the orientation of vertical printing, the printer's resolution is mainly determined by the nozzle width (which is fixed). Also, having more than 3 variations in beam thickness would result in too many test structures requiring too much testing time. Therefore, three beams with thicknesses of 1 mm, 2 mm and 3 mm were chosen to be printed and tested. This means that for both NinjaFlex and PI-ETPU, 3 beams with a length of 50 mm, height of 5 mm and widths of 1 mm, 2 mm and 3 mm were printed both horizontally and vertically and tested for their Young's modulus. In total, there were thus 12 different beams, 6 of NinjaFlex and 6 of PI-ETPU.

3.2.5 Measurements and Data Processing

After printing the test beams, first their actual dimensions were measured to see if they were printed as specified. These measurements were conducted with a digital calliper. The results were rounded to 1 digit, because flexibility of the material had a negative effect on the accuracy of the measurements. The specified and measured dimensions are shown in table 3.1.

Table 3.1: Specified and actual (measured) dimensions of beams used for determining the Young's modulus of NinjaFlex and PI-ETPU

Material & Print method	Specified dimensions $l \times w \times h$ [mm]	Measured dimensions $l \times w \times h$ [mm]
NinjaFlex, Horizontal	$50 \times 1 \times 5$	$49.2 \times 1.0 \times 5.1$
	$50 \times 2 \times 5$	$49.5 \times 1.9 \times 5.1$
	$50 \times 3 \times 5$	$49.6 \times 3.0 \times 5.1$
NinjaFlex, Vertical	$50 \times 1 \times 5$	$49.2 \times 1.0 \times 4.9$
	$50 \times 2 \times 5$	$49.4 \times 1.9 \times 4.9$
	$50 \times 3 \times 5$	$49.1 \times 2.9 \times 4.9$
PI-ETPU, Horizontal	$50 \times 1 \times 5$	$49.7 \times 1.1 \times 5.4$
	$50 \times 2 \times 5$	$49.7 \times 2.1 \times 5.3$
	$50 \times 3 \times 5$	$49.7 \times 3.1 \times 5.3$
PI-ETPU, Vertical	$50 \times 1 \times 5$	$50.2 \times 1.5 \times 5.1$
	$50 \times 2 \times 5$	$49.5 \times 2.0 \times 5.0$
	$50 \times 3 \times 5$	$49.5 \times 3.1 \times 5.0$

All beams were then tested as described in section 3.2.2. First, no-load data was obtained by performing a 50 second measurement without anything attached to the measurement setup. This resulted in an average displacement offset of ≈ -1.2 mm and an average voltage offset of ≈ 0.8 mV as shown in figure B.2. The average displacement and voltage of the no-load measurement were subtracted from all NinjaFlex and PI-ETPU measurements to remove measurement offsets induced by the measurement setup itself. The measurements for all NinjaFlex structures were conducted twice. For PI-ETPU only the 3 mm thick horizontally and vertically printed structures were tested twice. Figures B.3 and B.4 show these measurements in displacement vs time and force vs time. The data in these figures is not raw, because equation 3.8 was used to calculate the force and the no-load data was used to remove offsets.

From the sets of data shown in figures B.3 and B.4, the Young's modulus was determined by performing the following steps:

- Calculate stress σ .
 - Use Poisson's ratio ($\nu = 0.48$) and the dimensions in table 3.1 for L_0 , w_0 and h_0 together with the displacement measurements to determine the change in area for both NinjaFlex and PI-ETPU.
 - Use the resulting area to calculate the stress with equation 3.2.
- Calculate strain ε by using equation 3.3, length L_0 from table 3.1 and the change in length from the deflection measurements.
- Excluding data.
 - In figure B.3a two clipping values can be seen; one for $w = 1$ mm, horizontal print at $t \approx 0$ s and one for $w = 1$ mm, vertical print at $t \approx 550$ s. These are the clipped values of the displacement sensor as was mentioned in section 3.2.2. The clipped values do not actually hold true and are omitted by excluding both the first measurement of the 1 mm horizontal print and the first measurement of the 1 mm vertical print entirely. In all further results, of the first measurement the data of the 2 mm and 3 mm horizontal and vertical prints were used and of the second measurement the data of the 1 mm horizontal print and 1 mm vertical prints were used. Thus, also the data of the second measurement of 2 mm and 3 mm horizontal and vertical prints were excluded.
 - In figures B.3 and B.4 it can be seen that for most measurements, at the instant the jump to the second measurement step is taken (at $t \approx 25$ s), no significant changes with respect to the previous step are present. In those cases, the beam is not yet properly pulled by the voice coil. Therefore, this data (data points in the first two steps) was expected not to be very useful and was excluded. Something similar happens at the end of the measurement, where the voice coil reaches its limit. Also here, the final two steps were excluded.
 - In figures B.3 and B.4 it can also be seen that each step experiences some relaxation time. This movement towards an equilibrium for each step is especially visible in the force measurements. The path to reaching this equilibrium depends on a combination of factors influenced by both the measurement setup and the beam that is being tested. The eventual equilibrium point being reached is predominantly determined by the beam being tested and not by the measurement setup, so this point is of most interest. Therefore, only the 10 data points before the last data point (out of 50 points in total) were used. The first 40 data points for each step are excluded. The last data point was excluded, because it already measured the transition to the next step. An average is taken over the remaining 10 data points to yield an approximate value.

- Plot the stress versus the strain and their 4th order polynomials in figure B.5. The polynomial fits have been extended to approximate what the stress vs strain curves would look like. From these graphs it can be seen that the curves, if extended, would not originate from the graphs origin. This is due to the fact that the structures were put in the measurement setup manually. This caused each structure to be clamped under a different tension. The voice coil should have been pushed forward or backward slightly for each measurement to start at a force of 0 N. This has unfortunately not been done. To compensate for these deviations, the polynomial fits were used to check at what magnitude of strain no stress ($\varepsilon = 0$) should be present. The value for strain accompanying each zero-stress intersection was manually read and then subtracted from each according measurement. Now, if extended, the curves would approximately originate from the origin of the graph. This can be seen in figure 3.6 at the end of this section. The polynomial fits are as described in equation 3.9, where n equals the order of the polynomial fit and p represents the coefficients (MathWorks).

$$p(x) = p_1x^n + p_2x^{n-1} + \dots + p_nx^1 + p_{n+1}x^0 \quad (3.9)$$

The coefficients that were used in the polynomial fits in figure B.5 are given in tables A.2 (NinjaFlex) and A.1 (PI-ETPU).

- Finally, the measured Young's modulus of NinjaFlex and PI-ETPU was determined by dividing the stress by the strain and plotting it against the strain. This yielded the absolute Young's modulus, i.e. the Young's modulus at each value for strain with respect to the origin. Additionally, the change in stress divided by the change in strain is used to determine a relative Young's modulus as shown in equation 3.10. In this equation n represents a data index and $n - 1$ corresponds to the previous data point.

$$E_{rel}[n] = \frac{\sigma[n] - \sigma[n-1]}{\varepsilon[n] - \varepsilon[n-1]} \quad (3.10)$$

The resulting absolute and relative Young's modulus of NinjaFlex and PI-ETPU are shown in figures 3.4 and 3.5, respectively.

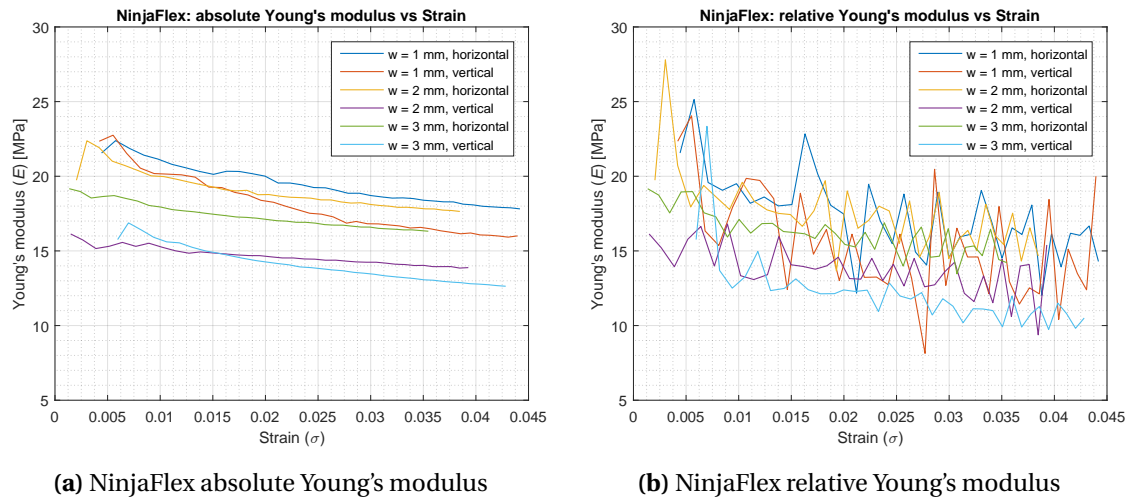


Figure 3.4: NinjaFlex absolute and relative Young's modulus measurement

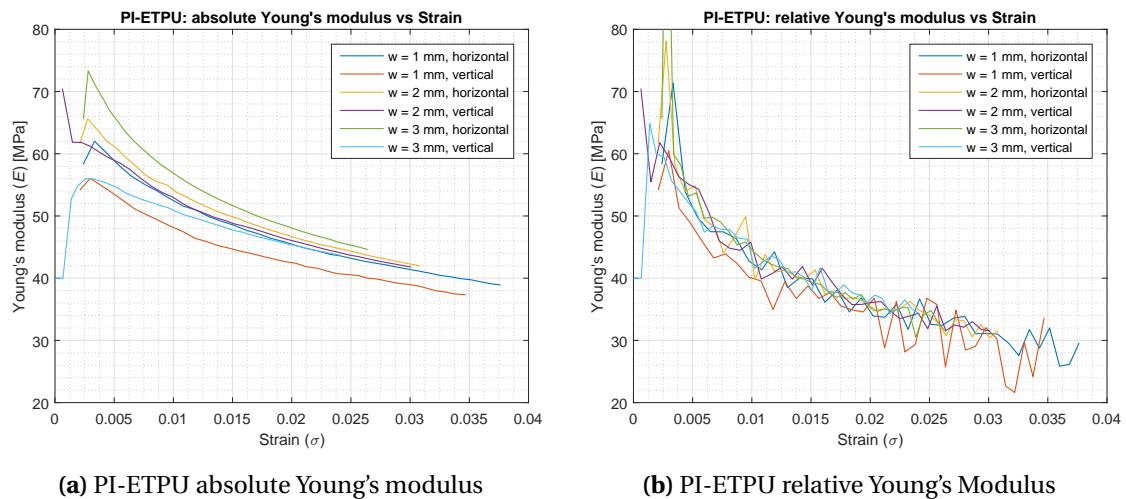
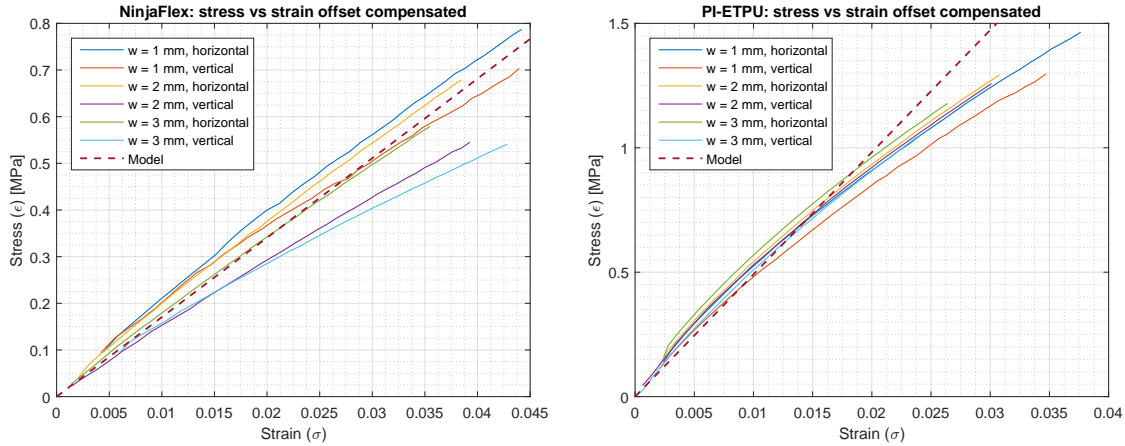


Figure 3.5: PI-ETPU absolute and relative Young's modulus measurement

To give a quick indication of the Young's modulus, for each plot the average Young's modulus was determined. The average Young's moduli are as follows:

- Average absolute Young's modulus of NinjaFlex ≈ 17.0 MPa.
- Average relative Young's modulus of NinjaFlex ≈ 15.4 MPa.
- Average absolute Young's modulus of PI-ETPU ≈ 49.1 MPa.
- Average relative Young's modulus of PI-ETPU ≈ 40.7 MPa.

By using the measured average absolute Young's moduli in the model, a comparison stress versus strain plot was made between the model and the measurements. This is shown in figure 3.6. Note that these plots also show the effect of removing the strain offsets.



(a) NinjaFlex modeled and measured stress versus strain

(b) PI-ETPU modeled and measured stress versus strain

Figure 3.6: Measured stress versus strain and modeled stress versus strain derived from the measured average absolute Young's moduli of NinjaFlex and PI-ETPU

3.3 Resistivity and Surface Resistance

3.3.1 Theory and Method

The electrical resistivity is a material specific property and can be used to estimate the electrical resistance of a certain object. It relates the resistance of an object to its length, width and height as described in equation 3.11.

$$R = \rho \cdot \frac{L}{w \cdot h} \quad (3.11)$$

The resistivity of NinjaFlex is assumed to be infinite. The volume resistivity of PI-ETPU 95-250 Carbon Black is $<300 \Omega\text{cm}$, according to the material info provided by the manufacturer (20). However, as was discussed in section 3.2.1, printed PI-ETPU is anisotropic. This means that the electrical resistance could differ within a structure itself and it could also differ per printed structure. To check the resistivity provided by the manufacturer, a measurement was conducted to redetermine the resistivity of PI-ETPU.

In section 2.3 it was specified that the FSR sensor being designed experiences a change in resistance due to a change in contact area. Therefore, measurements were conducted to determine the surface resistance between two sheets of PI-ETPU. Four-terminal sensing was applied in all electrical resistance measurements. This method was used to eliminate the contact resistance between the probes of an ohmmeter and the material it measures. The method is named four-terminal sensing, because two terminals are used to deliver a known fixed current to a material and two terminals are used to consequently measure the voltage across a section of the material where the input current flows through. A schematical drawing of four-terminal sensing is given in figure 3.7.

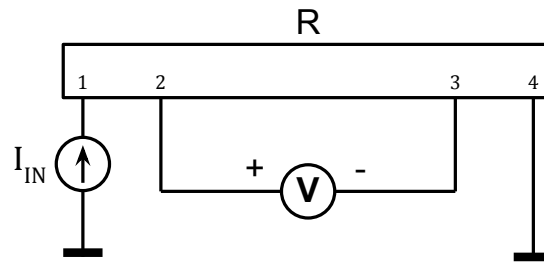


Figure 3.7: Electrical circuit schematic of four-terminal sensing

As input current I_{IN} is known, the resistance between 2 and 3 can be determined from the voltage measurement simply via Ohm's law.

3.3.2 Design

Figure 3.8 shows the top view of the structure that was designed to measure the resistivity of PI-ETPU.

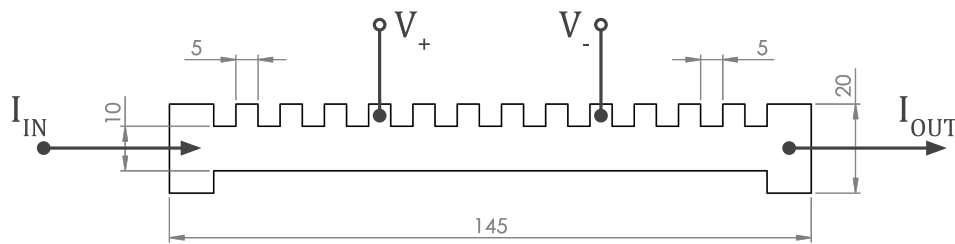


Figure 3.8: Top view and dimensions [mm] of resistivity testing structure

The resistance over several intervals was measured. Input current I_{IN} and output current I_{OUT} are known and equal. The contacts pads shown at the top of the design were included to have electric copper wires molten into them to form the contacts to the voltmeter. V_+ and V_- show an example of where the voltage could be measured. The contact pads all have the same fixed distance of 5 mm between them. This allows the resistance to be measured at multiple distances across the PI-ETPU structure. The resistance was measured over all possible distances between the contact pads.

Also structures to test the surface resistance of PI-ETPU with were designed. Multiple plates of different sizes were used to measure the resistance as a function of contact area. Figure 3.9 shows a schematic drawing of how the surface resistance is measured with four-terminal sensing. Two individual plates of PI-ETPU with a different area (length \times width) are placed on top of each other. The area of the smallest plate equals the contact area between the two plates.

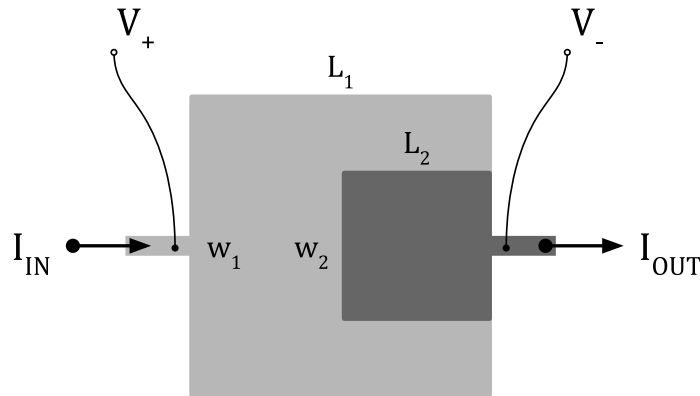


Figure 3.9: Schematic top view of two PI-ETPU plates placed on top of each other for measuring their surface resistance

In all plates used, the length equals the width, i.e. $L_1 = w_1$ and $L_2 = w_2$. The bottom structure will be the largest one. Table 3.2 shows the specified dimensions of the designed structures. All structures have a contact pad for electrical connection to the current source and ohmmeter attached to them. In all structures, this contact pad has the same dimensions. Its length equals 10 mm and its width equals 2 mm.

3.3.3 Measurements and Data Processing

First of all the dimensions of the structure in figure 3.8 were checked. The specified length of 145 mm was measured to be 144 mm. The path width, where the current flows through, was specified as 10 mm and measured as 10.25 mm. The height of the structure was specified as 2 mm and measured to be 1.95 mm.

Resistance measurements of the structure were manually conducted with a multimeter that has the option to do four-terminal sensing. It was assumed that the distance over which has been measured was the distance between the centres of the contact pads as specified, i.e. 10 mm between the centre of each neighbouring contact pad. There are 12 contact pads in total, so the largest distance to be measured over was $11 \times 10 \text{ mm} = 11 \text{ cm}$. The results of the resistance measurement, including an approximation, are shown in figure 3.10a. The approximation is given in equation C.1 and is a linear function without offset. The multiplication factor in this function was determined by dividing the average measuring distance by the average measured resistance. It must be noted that during any single measurement, as time passed, the resistance shown on the multimeter kept decreasing. Trying a different multimeter also showed a decrease over time. The decrease in resistance over time did gradually decline. The measurements shown in 3.10a were taken after waiting for approximately 5 to 10 minutes, when the resistance settled more or less.

The resistivity was determined with equation 3.11, where L equals the specified distances between the centres of the contact pads, w and h equal the above mentioned measured width and height, respectively, and R equals the measured resistance as shown in figure 3.10a. The resistivity resulting from both the resistance data points and the approximation is plotted against the measurement distances in figure 3.10b.

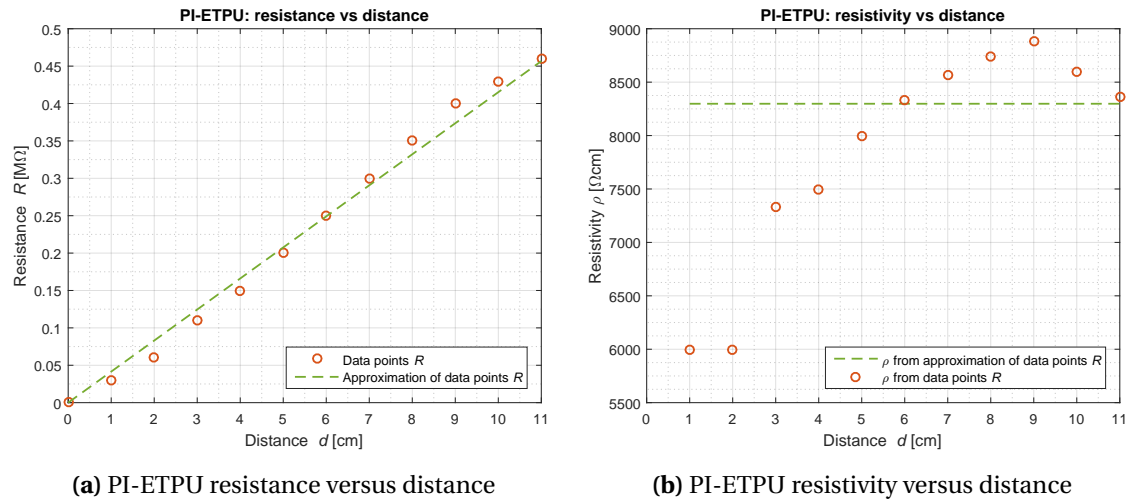


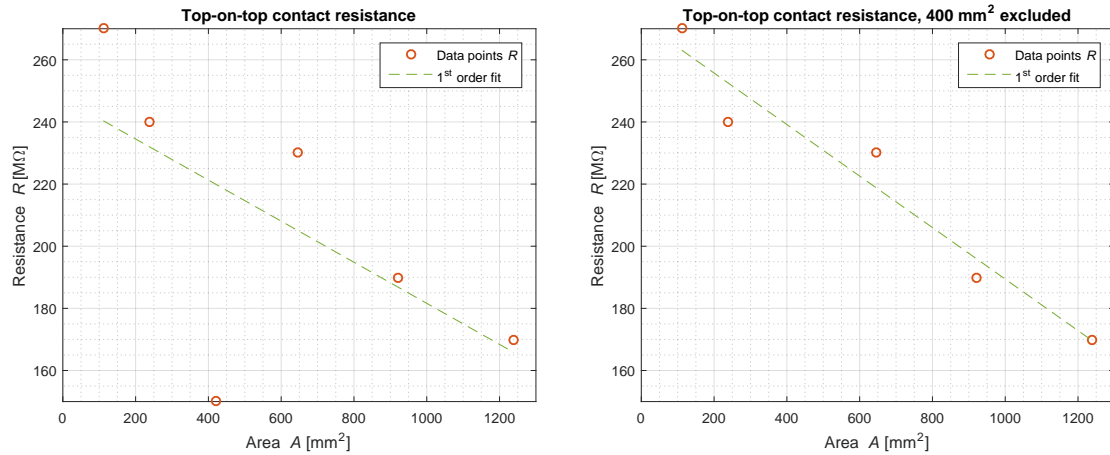
Figure 3.10: PI-ETPU measured resistance and resistivity over increasing distances on the structure shown in figure 3.8

Before conducting the surface resistance measurements, again the dimensions of the testing structures were checked. Table 3.2 shows the dimensions of the plates as specified and measured.

Table 3.2: Specified and actual (measured) dimensions of the testing plates used for determining the surface resistance of PI-ETPU

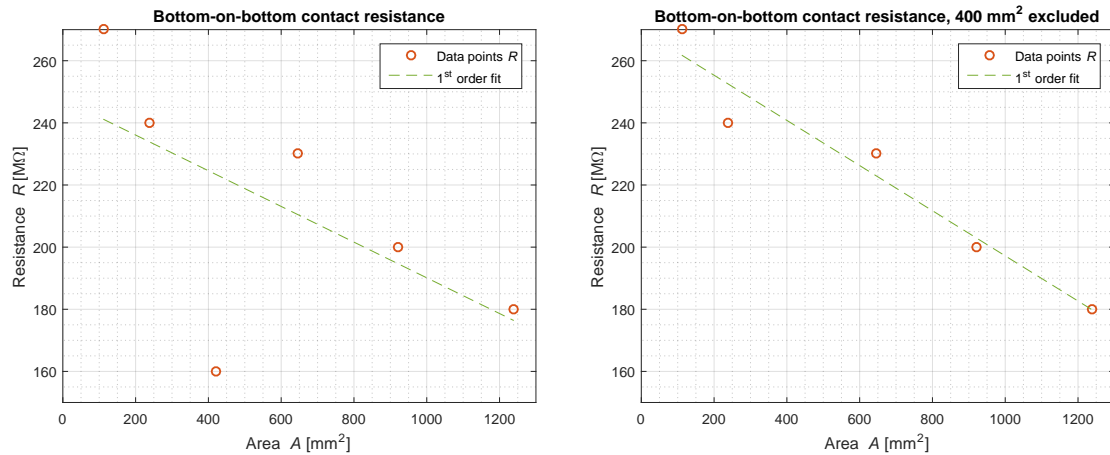
Plate #	Specified dimensions $l \times w \times h$ [mm]	Specified area A [mm ²]	Measured dimensions $l \times w \times h$ [mm]	Measured area A [mm ²]
0 (Base)	$40 \times 40 \times 0.4$	1600	$40.1 \times 40.2 \times 0.6$	1612.02
1	$35 \times 35 \times 0.4$	1225	$35.2 \times 35.2 \times 0.6$	1239.04
2	$30 \times 30 \times 0.4$	900	$30.4 \times 30.3 \times 0.6$	921.12
3	$25 \times 25 \times 0.4$	625	$25.4 \times 25.4 \times 0.6$	645.16
4	$20 \times 20 \times 0.4$	400	$20.5 \times 20.5 \times 0.6$	420.25
5	$15 \times 15 \times 0.4$	225	$15.5 \times 15.4 \times 0.5$	238.70
6	$10 \times 10 \times 0.4$	100	$10.6 \times 10.5 \times 0.6$	111.30

Plate 0 was used as the bottom plate during all measurements. This means that L_1 and w_1 (figure 3.9) are always 40.1 and 40.2 mm, respectively. Thus, L_1 and w_1 depend on which of the six remaining contact plates is placed on top of the base plate. All resistance measurements were conducted manually with a multimeter. During the measurements a fixed (nonconductive) weight of approximately 0.5 kg was pushing down on the plates to ensure proper contact between them. Figure 3.11 shows the results of the resistance versus contact area measurements.



(a) Resistance where the top sides of the PI-ETPU plates are in contact

(b) Resistance where the top sides of the PI-ETPU plates are in contact and the 400 mm² surface resistance is excluded



(c) Resistance where the bottom sides of the PI-ETPU plates are in contact

(d) Resistance where the bottom sides of the PI-ETPU plates are in contact and the 400 mm² surface resistance is excluded

Figure 3.11: PI-ETPU contact area resistance measurements where the top sides of the plates are in contact with each other and where the bottom sides of the plates are in contact with each other

The bottom and top sides of the 3D-printed PI-ETPU plates differ in texture. The bottom layer, which was printed directly on the heated bed of the 3D-printer, is significantly more smooth than the top layer, which is more rough. To see if this makes a difference in measuring surface resistance, measurements were taken where both the top sides of the plates are in contact (figure 3.11a) and where both the bottom sides are in contact (figure 3.11c). During the measurements, there were troubles measuring the surface resistance with the 400 mm² plate. In most measurement attempts, no resistance could be measured at all (infinite resistance). This only was the case with the 400 mm² area plate, no such issues were recorded while measuring the other contact plates. It could be the case that the measurements that did succeed with this plate are not accurate. Therefore, figures 3.11b and 3.11d were made in which the resistance measurement corresponding to the 400 mm² plate is excluded. The first order polynomial fits shown in figures 3.11a, 3.11b, 3.11c and 3.11d are specified by appendix equations C.2, C.3, C.4 and C.5, respectively.

3.4 Discussion

3.4.1 Young's Modulus and Poisson's Ratio

Figure 3.5 shows the Young's modulus changing along the magnitude of elongation of the material. This change is more present in PI-ETPU, which starts at a Young's modulus of about 60 MPa and declines to about 30 MPa, than it is in NinjaFlex, which starts slightly above 15 MPa and declines to about slightly below 15 MPa. Thus, these measurements were (partly) conducted above the linear limit of the Young's modulus. The Young's moduli provided by the manufacturers is 12 MPa for both NinjaFlex and PI-ETPU (18; 20). The results shown in figure 3.5 indicate a significant difference between the specified and measured Young's moduli. If we look at the relative Young's modulus, then the average measured Young's modulus of NinjaFlex is 28% larger compared to the datasheet specification. The average Young's modulus of PI-ETPU has been measured to be 239% larger than claimed by the manufacturer. What causes these differences? In section 3.2.1 it was stated that the Young's modulus of a structure can vary depending on under which conditions and printing settings it is printed. The NinjaFlex datasheet states that the D638 standard tensile test method for plastics was used. Also, a drawing is provided of the testing structure used to determine the Young's modulus of 12 MPa. The length and height of this structure (33 mm and 6 mm, respectively) (18; ASTM International) that were tested are slightly different from those used in this research (50 mm and 5 mm). Also, the D638 standard test method for the tensile properties of plastics does differ from the method used in this research. The datasheet of PI-ETPU also indicates that the ASTM D638 method was used to determine the tensile modulus. Furthermore, it states that "The information in this data sheet represents typical values for the original standardized sample and should not be regarded as a fixed specification for all filaments. 3D-printing will affect these values" (20). This indicates that the measured Young's modulus may very well be different from the specified one. The steps applied in this research to determine the Young's modulus from the measurement data include the assumption of a (fixed) Poisson's ratio, the removal and averaging of certain data and the manual removal of strain offsets based on a polynomial curve fitting. All of it contributes to the difference in the specified and measured Young's modulus of NinjaFlex and PI-ETPU. Especially the removal of strain offsets by looking at a polynomial curve fittings is highly disputable, because these do not capture the stress-strain relations well. Perhaps a linear approximation below the linear limit of the Young's modulus would have sufficed. Though, it must be noted that the difference in the specified and measured Young's modulus of PI-ETPU is significant to say the least.

Another interesting note is that the Young's moduli of the horizontally printed beams are only slightly larger than those of vertically printed beams. These differences were expected because of the different layer-on-layer buildups of these beams. However, the measurements indicate that these differences are not significant.

In figure 3.6 the modelled and measured stress is plotted versus the strain. In figure 3.6a for NinjaFlex we can see that the modelled curve remains close to the measured values. This is because the measurements do not display much of a curvature. If the Young's modulus of each individual structure was taken, the model would have come close to the individual measurements. Things are different in the case of PI-ETPU, where the measurements show a decreasingly steep slope. Deviation from the model starts to significantly increase for strains greater than 0.02. This is due to the Young's modulus of PI-ETPU not being constant; it decreases for increasing strain.

The Poisson's ratio of both NinjaFlex and PI-ETPU was assumed to equal 0.48 following some literature. Ideally, this would have also been measured during this research. It could be that the

Poisson's ratio of NinjaFlex and PI-ETPU is different and it could also be that the Poisson's ratio is varying depending on the strain. However, looking at equation 3.7 and assuming that the actual Poisson's ratio does not significantly differ from 0.48, we can see that for small strains the Poisson's ratio does not have a significant influence on the Young's modulus. This was also proven by changing the Poisson's ratio to values tenfolds larger than 0.48, which are not physically possible, in the MATLAB simulations and not seeing significant changes.

3.4.2 Resistivity and Surface Resistance

The resistance and resistivity versus distance measurements of figure 3.10 resulted from measurements that were conducted of the structure in figure 3.8. The measurements on this structure rely on the principle that the voltage at a certain horizontal distance parallel to the flow of current, x , should be the same regardless of the vertical position y perpendicular to the flow of current. This is based on the assumption that the internal resistance of the structure is equal throughout the structure, so that the flow of current is equally spread throughout the structure. However, as mentioned, 3D-printed TPU is not isotropic and so it could be that the current flow is not equally spread throughout the structure and therefore the resistance measurements may not be fully accurate. The results of the resistance and resistivity versus distance measurements as shown in figure 3.10 indicate that the resistance versus distance relation is nearly linear, which would be as expected. It was assumed that the measuring distance was exactly between the centre of two contact pads. However, the wires molten into these contact pads were spread with a certain width, making the distances shorter by a couple of millimetres than accounted for in figure 3.10. This could explain some of the deviations (slight offset to the right) of the measuring points from the linear approximation and in result the non-constant resistivity derived from the resistance data points.

According to the datasheet provided by the manufacturer, the volume resistivity of PI-ETPU 95-250 Carbon Black is $<300 \Omega\text{cm}$ (20). However, the approximation that was derived from the measurements indicates a resistivity of $\approx 8.3 \text{ k}\Omega\text{cm}$, which is 28 times larger. Again, this could be due to environmental conditions and anisotropy of the material, or as the manufacturer stated that "3D-printing will affect these values" (20). Also, the measurement method used in this research could be inaccurate or the multimeter could have given incorrect measurements, but as with the Young's modulus, the measured difference is of such a significant magnitude that one could wonder if the datasheet is correct. It is interesting to note that another datasheet of PI-ETPU 95-250 Carbon Black exists in which a volume resistivity of $<100 \Omega\text{cm}$ is indicated (21), suggesting that the manufacturer already once adjusted this value.

During the surface resistance measurements, plate 0 was used as the bottom plate for all measurements. Unfortunately, this means that for any plate placed on top of the bottom plate, the path length towards the contact area is different. A part of the measured resistance will thus result from this path and it will be different for each measurement. However, looking at the results of the just discussed resistivity measurements shown in 3.10, the order of magnitude of the path resistance is expected to be lower to such a degree that it is hardly significant in the measurement results shown in figure 3.11, which are of a significantly larger magnitude. The resistance measured for the 400 mm^2 contact pad was excluded from the data, as this measurement provided troubles while measuring and the measurement was not in line with the others. This issue may indicate an underlying problem that could have to do with what was mentioned before, that the printed material is anisotropic and current flow may not be equally spread throughout the structure. If then the voltage measuring probes of the four-terminal measurement are placed at a location or layer where the current flow differs from elsewhere, a resistance could be read that does not hold as a general value for the structure. This is just

a suggestion and may not hold true, because the results in figure 3.10 do yield consistent results. The surface resistance measurements with the 400 mm² contact pad excluded indicate a relatively large surface resistance in the range of 170 to 270 MΩ for contact areas between 100 and 1300 mm², which is a range of areas larger than the area of a fingertip. Furthermore, the results show no significant differences between the top-on-top and bottom-on-bottom measurements. The top-on-top measurements seem to have a slightly steeper decline in resistance for increasing area, but given the manual resistance readouts and inconsistent waiting times between readouts, this can not be stated with certainty. Also a fixed weight of approximately 0.5 kg was used to press down on the plates. This causes a difference in pressure depending on the area of the plate. A smaller plate will experience a greater pressure than a larger plate. This could have influenced the measurements.

As a final note, all resistance measurements were manually conducted four-terminal measurements with a multimeter. Non-manual measurements, where the data would be digitally logged to a computer, could have given more insightful and more accurate data. This was not done to save time, because no such setup was readily available.

3.5 Conclusion

This chapter elaborated on the research conducted on the Young's modulus and Poisson's ratio of NinjaFlex and PI-ETPU and the volume resistivity and surface resistance of PI-ETPU. The Poisson's ratio was not measured. Instead, it was assumed that the Poisson's ratio of NinjaFlex and PI-ETPU equals 0.48. According to their datasheets, the Young's modulus of both NinjaFlex and PI-ETPU equals 12 MPa. The measurements conducted during the research yielded a resulting average absolute Young's modulus of 17.0 MPa and 49.1 MPa and an average relative Young's modulus of 15.4 MPa and 40.7 MPa for NinjaFlex and PI-ETPU, respectively. Especially for PI-ETPU this is a significant difference compared to the datasheet provided by the manufacturer. These differences may be (partly) due to the printing of the material, the method of measuring and the data processing. Additionally, it was found that the Young's moduli of horizontally and vertically printed beams do not significantly differ.

The resistivity of PI-ETPU is <300 Ωcm according to its datasheet. In the conducted measurements a resistivity of ≈ 8.3 kΩcm was found, which is 28 times larger. Again, this is a significant difference measured on PI-ETPU compared to the specification provided by the manufacturer. The surface resistance was measured to be in the range of 170 to 270 MΩ for contact areas between 100 and 1300 mm². One measurement was excluded, because it caused difficulties during the measurements and it was not in line with the other measurements. Both bottom-on-bottom and top-on-top contact measurements were conducted on surface resistance, because these differ in surface texture. However, no significant differences were found in the surface resistance measurements for the bottom-on-bottom and top-on-top contact measurements.

4 Sensor Modelling and Design

4.1 Introduction

With the Young's moduli of NinjaFlex and PI-ETPU known, modelling and designing of the actual sensor started off. In chapter 2 the decision was made to design an FSR sensor. An indication was already given that the sensor could consist of two plates of PI-ETPU above each other. The contact area between these plates would then increase by applying a force. Consequently, the resistance would decrease following the increasing contact area. As discussed in section 1.3, one of the subgoals in this research was to design a fingertip strain sensor that is as small as possible. Also, the sensor should be producible in a single 3D-print without requiring any further assembly. These goals are to be taken into account when designing the sensor. This chapter describes the modelling and designing of the 3D-printed flexible fingertip strain sensor.

4.2 Model

The model is based on two plates above each other with spacers in between, as shown in figure 4.1.

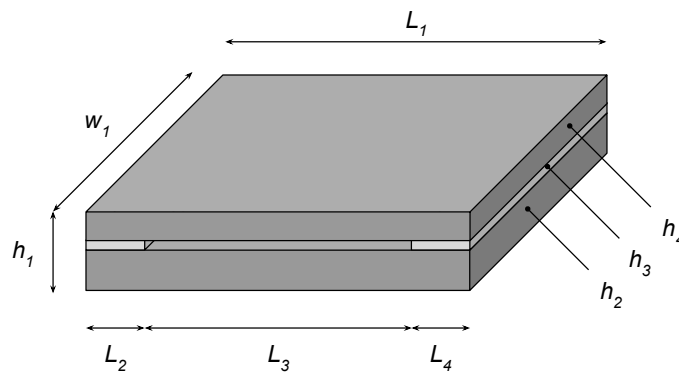


Figure 4.1: Graphical representation of the model with labelled dimensions

The two plates (dark grey) above each other are conductive PI-ETPU. The two spacers (light grey) on either side are nonconductive NinjaFlex. Having a space between the two PI-ETPU plates means that there is a threshold force at which the plates make their first contact. Assuming the bottom plate is laying on a flat surface and the top plate is pushed down upon by an equally spread load, the threshold force will be mainly determined by the height (thickness) of the spacers (h_2) and the height of the top plate (h_4). For a fingertip force sensor in general, it would be preferred to have the threshold force as low as possible so that forces as small as possible can be measured. This is why the spacers are modelled on two opposite sides and not all around; to obtain a lower threshold force.

The average absolute Young's moduli for NinjaFlex (17.0 MPa) and PI-ETPU (49.1 MPa) found in chapter 3 are implemented in the model. The model considers the sensor to be positioned on a flat rigid surface. The top plate is assumed to be bending. The spacers are assumed to be compressible, but not bending. The bottom plate is not accounted for in the model, which is similar to assuming the bottom plate to be rigid. Depending on how the sensor will be printed, it can either be simply- or rigidly supported. The sensor would be simply supported if the top plate is touching, but not attached to the spacers and it would be rigidly supported if the top plate is physically attached to the spacers.

In case of a rigidly supported top plate, equation 4.1 can be used to determine the deflection of the top plate, D_p , at any position, $x \leq \frac{1}{2}L_3$, along the length of the sensor for a uniform load, W (CodeCogs). In case of a simply supported top plate, equation 4.2 could be used (CodeCogs).

$$\text{Rigidly supported:} \quad D_p(x) = \frac{W \cdot x^2}{24 \cdot E \cdot I \cdot L_3} (L_3 - x)^2 \quad (4.1)$$

$$\text{Simply supported:} \quad D_p(x) = \frac{W \cdot x (L_3 - x)}{24 \cdot E \cdot I \cdot L_3} (L_3^2 + x(L_3 - x)) \quad (4.2)$$

In these equations, I represents the second moment of inertia and is described by equation 4.3 (15), where w_1 and h_4 represent the width and height indicated in figure 4.1, respectively.

$$I = \frac{1}{12} w_1 \cdot h_4^3 \quad (4.3)$$

For now a rigidly supported top plate is assumed. Combining equations 4.1 and 4.3 yields equation 4.4.

$$D_p(x) = \frac{W \cdot x^2}{2 \cdot E \cdot L_3 \cdot w_1 \cdot h_4^3} (L_3 - x)^2 \quad (4.4)$$

Spacer compression is also accounted for. For this we can rewrite equation 3.4. For ease of implementation, equation 3.4 is used instead of equation 3.7. If the forces are small enough, the compression (ΔL in equation 3.7) will be small enough for it to not make a significant difference between the two equations. After rewriting equation 3.4 and implementing the dimensions of figure 4.1, equation 4.5 for the compression of the spacers, D_s , is obtained. A division by 2 is added, because the load is spread over two spacers.

$$D_s = \frac{W \cdot h_3}{2 \cdot L_2 \cdot w_1 \cdot E} \quad (4.5)$$

We can now calculate the distance between the bottom plate and the top plate, y_p , at any position, $x \leq \frac{1}{2}L_3$, along the length of the model. This can be done by taking the original spacer height and subtracting it with the deflection of the top plate and the compression of the spacers. The result is shown in equation 4.6.

$$y_p(x) = h_3 - (D_p(x) + D_s) \quad (4.6)$$

Obviously, this distance cannot be negative, so equation 4.6 is rewritten into equation 4.7. Note that this does not take into account that the plates are now actually touching, which would change the physical behaviour of the sensor.

$$y_p(x) = \begin{cases} h_3 - D_p(x) - D_s, & \text{if } D_p(x) + D_s < h_3 \\ 0, & \text{if } D_p(x) + D_s \geq h_3 \end{cases} \quad (4.7)$$

If we want to know $y_p(x)$ at $\frac{1}{2}L_3 < x \leq L_3$ we can simply mirror the equation, as shown in equation 4.8.

$$y_p(x) = \begin{cases} h_3 - D_p(x) - D_s, & \text{if } D_p(x) + D_s < h_3 \quad \text{and} \quad 0 \leq x \leq \frac{1}{2}L_3 \\ 0, & \text{if } D_p(x) + D_s \geq h_3 \\ h_3 - D_p(L_3 - x) - D_s, & \text{if } D_p(L_3 - x) + D_s < h_3 \quad \text{and} \quad \frac{1}{2}L_3 < x \leq L_3 \end{cases} \quad (4.8)$$

By assuming some realistic example dimensions given in table 4.1, a plot could be made. Realistic means taking into account the size of a fingertip and the resolution of the 3D-printer.

Table 4.1: Dimensions of the model shown in figure 4.1 used for plotting the plate distance shown in figure 4.2

L_1 [mm]	$L_2 = L_4$ [mm]	$L_3 = L_1 - L_2 - L_4$ [mm]	w_1 [mm]	h_3 [mm]	h_4 [mm]
5	1	2	2.5	0.4	0.4
5	1	2	2.5	0.4	0.6
5	1	2	2.5	0.4	0.8

Figure 4.2 shows the distance between the top plate and the bottom plate, where the top plate is represented by the coloured curves and the bottom plate is considered to be at 0 distance.

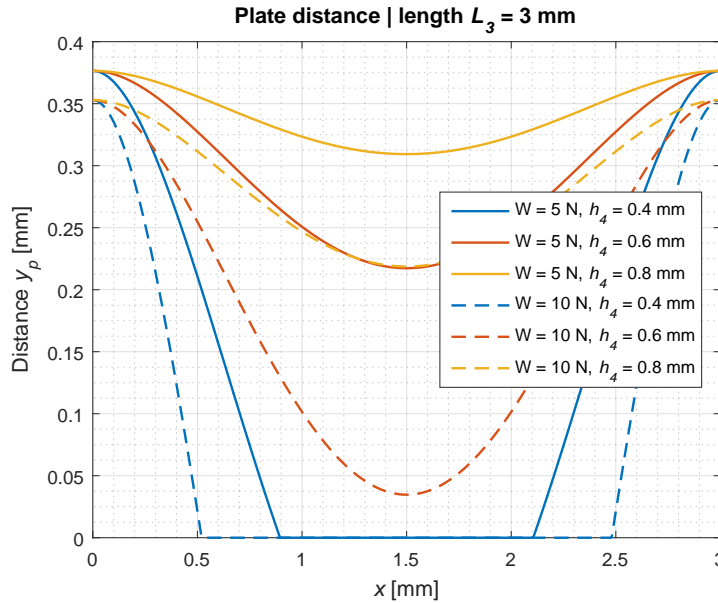


Figure 4.2: Modeled plate distance for 2 forces and for beams of various heights specified in table 4.1

Now the contact area, A , versus applied load, W , could be predicted. The contact area can be determined by first finding x for which equation 4.6 equals 0. The outcoming value of x , x_{contact} , should then be subtracted from half the plate length, $\frac{1}{2}L_3$, and the whole should be multiplied by 2, because of symmetry around the centre. This would thus yield equation 4.9.

$$A = 2 \cdot \left(\frac{1}{2}L_3 - x_{\text{contact}} \right) \cdot w_1 \quad (4.9)$$

Instead of finding x_{contact} by solving equation 4.6 for $y_p(x) = 0$, MATLAB was used to find x_{contact} . A logarithmic plot of contact area versus the applied load is given in figure B.7.

With the resistance versus area approximation found in chapter 3, figure 3.11b, an estimation of force versus resistance can be made. The top-on-top approximation was taken, because a sensor printed in practice will have contact plates with the same texture. The resistance approximation found in chapter 3 is given in equation 4.10, with resistance R [Ω] and area A [m^2].

$$R(A) \approx (-82.9 \cdot A + 0.27) \cdot 10^9 \quad (4.10)$$

Finally, the resistance can be determined as a function of applied force or load, W , which is shown logarithmically in figure 4.3.

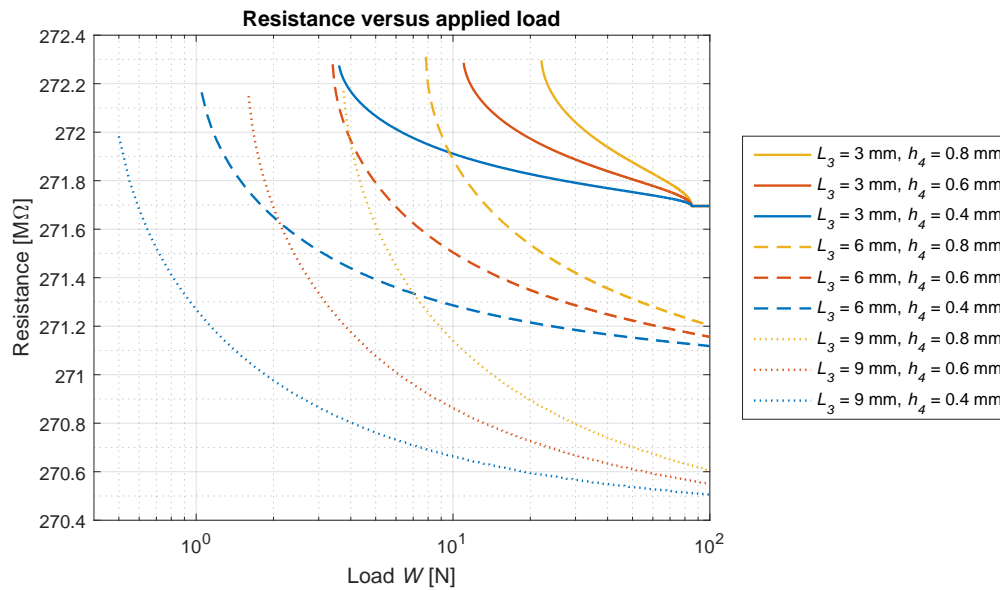


Figure 4.3: Sensor model logarithmic plot of contact area versus applied load for various top plate lengths and heights

4.3 Design

Many attempts were made to try and print a sensor with physical properties similar to the model shown in figure 4.1 in a single print, with all structures attached to each other (that is, the spacers attached to both the bottom and top plate). Unfortunately, all of these attempts have failed. The dimensions regarding length and width, i.e. L_1 , L_2 , L_3 , L_4 and w_1 , were well printable, but the dimensions regarding height were not. Referring to the terminology of 'horizontal printing' and 'vertical printing' introduced in section 3.2.4, various horizontal and vertical prints were made with various values for h_2 , h_3 and h_4 . In horizontal printing, there were no problems printing height h_2 , but the top plate was only possible to bridge between the two spacers for a large spacer height, h_3 , in combination with a small bridging length, L_3 . This would result in a sensor that could never be used as a fingertip force sensor, because A) the top and bottom plate could never touch, because of the small length L_3 and the large height h_3 and B) the goal of making a small sensor would not be achieved. In vertical printing, it was also the heights h_2 , h_3 and h_4 that caused trouble. The nozzle width of the extruder imposed a minimal value on these heights, that was too large. This would also make the sensor too big and too stiff.

To avoid the above-mentioned problems, a new foldable design was developed. Herein, the top plate is not attached to the spacers. The design is shown in figure 4.4 with labelled dimensions. Note that from here on the dimension as labelled in this figure will be referred to.

This design can be printed properly, because it requires no bridging of TPU and its total height is kept low. Twelve of these sensors are printed in different sizes to see what dimensions are achievable and to compare performance of sensors with different dimensions. The printer settings used for all twelve sensors are listed in table A.3. At the basis are three different area sizes (A, B and C), shown in figure B.8. These are actual designs that were sent to the 3D-printer. Table 4.2 gives an overview of the dimensions of the 12 different sensors. For all 12 sensors, the following holds:

- $w_1 = L_1 = L_2$
- $w_2 = w_1 - 2.5 \text{ mm}$
- $h_1 = h_2 = h_r = h_b$
- $L_s = 1.2 \text{ mm}$
- $L_r = 15 \text{ mm}$
- $w_r = 1.2 \text{ mm}$
- $L_b = 62 \text{ mm}$
- $w_b = 3.9 \text{ mm}$

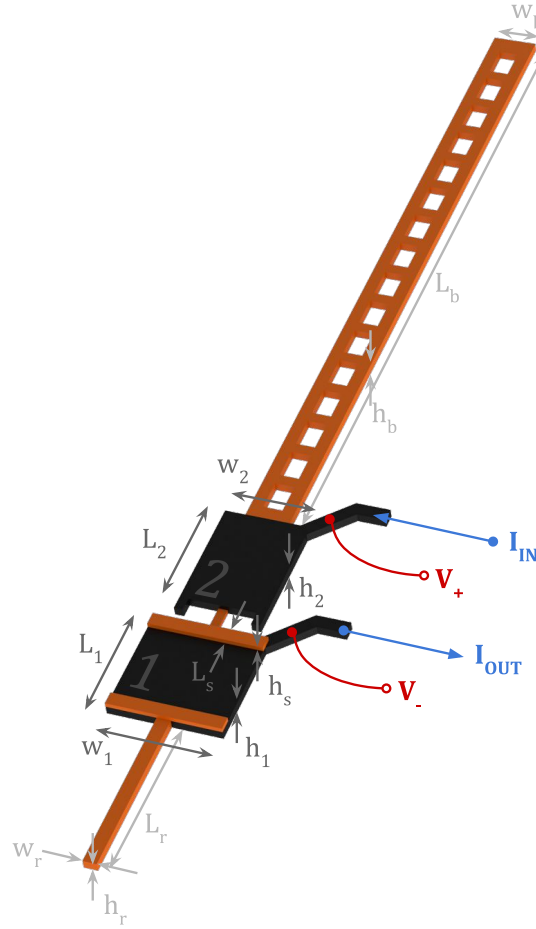


Figure 4.4: Foldable sensor design

Plate 1 is the bottom PI-ETPU plate on top of which 2 NinjaFlex spacers are printed. Plate 2 is the top plate and can be folded on top of plate 1 and the spacers. The width of plate 2 is 2.5 mm smaller than the width of plate 1, so that the top plate can shift a bit and still be aligned above plate 1 to make contact along its full width. When folded on top of each other, the rod and belt can be used to secure this folded position by pushing the rod through the first hole in the belt. Then the belt can be wrapped around the finger and the rod can be pushed through the belt one more time, fastening the sensor around the fingertip.

Table 4.2: Varying sensor dimensions resulting in 12 different sensors

Sensor	L_1 [mm]	h_1 [mm]	h_s [mm]
A1	10	0.8	0.4
A2	10	0.8	0.2
A3	10	0.6	0.4
A4	10	0.6	0.2
B1	7.5	0.8	0.4
B2	7.5	0.8	0.2
B3	7.5	0.6	0.4
B4	7.5	0.6	0.2
C1	5	0.8	0.4
C2	5	0.8	0.2
C3	5	0.6	0.4
C4	5	0.6	0.2

Plates 1 and 2 are attached to each other by a NinjaFlex beam of which the dimensions were determined by means of trial and error: length = 2.5 mm, width = 0.8 mm and height = 0.4 mm. The dimension of the rod (L_r , w_r and h_r) and the belt (L_b , w_b and h_b) were also determined after trial and error. The sizes of the rod and the holes in the belt are such that the rod must be twisted before it can be pushed through the holes in the belt. When the rod is pushed through a hole in the belt, it wants to twist back to its original shape, but the holes in the belt are not big enough to allow for that. This way, the rod clamps itself in the belt. Furthermore, each plate has a beam of PI-ETPU sticking out to connect electrical wires to. Four-terminal sensing is accounted for as indicated in figure 4.4. A picture of the sensor in practice is shown in figure B.9.

4.4 Discussion

The model was constructed with many of assumptions. First, an equally spread load is assumed. It is likely that this will often not be true in practice, where fingertips are used to grab objects of various shapes and sizes. The bottom plate as indicated in figure 4.1 is assumed to be on a flat rigid surface. This will not hold true for application on a fingertip, which is a non-flat compliant surface. It is assumed that the spacers will not bend. Even though their lengths (L_2 , L_4) and width (w_1) are significantly larger than their height (h_2), some bending of the spacers will still occur. The bottom plate is assumed to be flat and rigid. This will not hold true in practice, where the bottom plate will experience deflection and compression. Given the design of figure 4.4, the sensor will not be fully rigidly supported, nor will it be simply supported. The top plate is not attached to the spacers, but the belt will keep the top plate in place. Because the belt keeps it in place, the top plate will probably experience more of a rigid supported plate than a simple support. Equation 4.1 was used to determine the deflection of the top plate. This equation is based on Euler-Bernoulli beam theory and may not hold true for plate behaviour and large deflections. Also, equation 4.5 for estimating the compression of the spacers may not entirely hold true. For large deflections, the Poisson's ratio will start to have an influence and in that case an equation that takes into account the Poisson's ratio is required, like equation 3.7. When the distance between plates 1 and 2 reaches 0, the model does not take into account that the plates are actually touching and changing the physical behaviour of the top plate. Equation 4.7 is overly simplified. A proper model would take into account the changing physical behaviour at the moment the two plates are in contact. The current model can still be used to estimate the force at which the first point of contact between the top and bottom plate occurs. It can also be used to approximately estimate the contact area. The results will be a bit off due to the just mentioned shortcomings of the model. The results shown in figure 4.3 indicate only a small change in resistance that happens mainly in a small load interval. For the beams with $L_3 = 3$ mm a flat line can be seen at loads between 85 N and 100 N. This is because then the compression of the NinjaFlex spacers is modelled to be 100%, i.e. the spacer height then equals 0. At large loads like these the deflection of the top plate and compression of the spacers do not hold true.

Printing the sensor in a shape similar to model template shown in figure 4.1 failed to result in a structure that could meet the specified goal of making a small sensor. However, with the new design shown in figure 4.4 the subgoal of making a sensor that does not require an assembly is not achieved. It needs to be folded and manually strapped onto a fingertip by putting the rod through the belt. The design does meet other subgoals specified in section 1.3. It is novel, based on the most suitable transduction principle (FSR), can be made small and is producible in a single 3D-print. If a printer with smaller nozzle widths that could print NinjaFlex and PI-ETPU was available, one could attempt to make a single print by 'vertically' printing it. More ideally would be a printer that could make a bridging structure of PI-ETPU accurately to allow an FSR sensor to be 'horizontally' printed. Using supporting material could possibly help out here.

The foldable design of the sensor makes that the model deviates even more from the sensor. When folded, the small NinjaFlex beam that attaches plate 1 to plate 2, will exert an upward (and sideward) force on plate 2. Also, the belt will exert an additional force downward on plate 2, depending on how tightly the belt is strapped around a finger. This can intuitively be seen in the picture of figure B.9, where the belt visibly compresses the centre finger.

4.5 Conclusion

In this chapter the FSR sensor model and design were discussed. The model is based on two PI-ETPU plates on top of each other with NinjaFlex spacers in between. It has a lot of areas on which it could be improved, like the deflection equation for the top plate in general, the compression equation of the spacers for large compressions and the physical behaviour of the sensor from the moment the two plates make contact. Given its limitations, the model can be used to give an approximate estimation of the contact area or resistance change for small loads. The design of the FSR sensor considers a foldable sensor. It requires an assembly by putting a rod through a belt in order to fix the top plate above the spacers and in order to fasten the sensor around a finger. Therefore, the goal of making a sensor that does not require an assembly, which was stated in section 1.3, is not met. Otherwise, the other goals of designing a novel sensor that is based on the most suitable transduction principle (FSR), that can be made small and that is producible in a single 3D-print, are met.

5 Sensor Characterization

5.1 Introduction

To determine the performance of the designed sensor, it needs to be characterized. The resistance has been measured as a function of force for all 12 sensors. By comparing the sensor measurements to the model predictions, the performance of the model can also be assessed. Information can then be gathered on how to improve the model and thus the understanding of the sensor operation. In this chapter, first the measurement setup and model adjustments are explained. Then the measurement results are shown, followed by a discussion and conclusion.

5.2 Method

The measurement setup consists of a SMAC LCA25-050-15F programmable actuator in combination with a Keithley 2410 Source Measure Unit (SMU). The position or force applied by the actuator can be programmed versus time. Both can also be measured and digitally logged by the actuator's controller. The controller measures the distance in counts and the force with a (converted) resolution of 0.1 N in an interval of approximately 110 milliseconds. The sensor was clamped in a rigid structure in front of the actuator. The actuator was then force controlled to gradually push against the sensor. A picture of this setup is shown in appendix figure B.10. The control scheme is given in table 5.1. The amount of applied force is presented in percentages of the rated force. During the first 340 seconds a gradual slope of 0.5% per second towards the maximum force (80%) and back to zero force is ordered. In the interval of 345 to 425 seconds a staircase that goes to maximum force and back to zero force with steps of 20% is ordered.

Table 5.1: SMAC actuator control scheme that was used for the sensor measurements

Time [s]	Command
0 - 170	Force move: to 80% rated force Slope: 0.5%/sec
170 - 340	Force move: to 0% rated force Slope: -0.5%/sec
340 - 345	Position move: to 0 counts Velocity: 10000 counts/sec Acceleration: 50000 counts/sec ²
345 - 355	Force move: to 20% rated force Slope: 20%/sec
355 - 365	Force move: to 40% rated force Slope: 20%/sec
365 - 375	Force move: to 60% rated force Slope: 20%/sec
375 - 385	Force move: to 80% rated force Slope: 20%/sec
385 - 395	Force move: to 60% rated force Slope: -20%/sec
395 - 405	Force move: to 40% rated force Slope: -20%/sec
405 - 415	Force move: to 20% rated force Slope: -20%/sec
415 - 425	Force move: to 0% rated force Slope: -20%/sec
425 - 430	Position move: to 0 counts Velocity: 10000 counts/sec Acceleration: 20000 counts/sec ²
430 - 431	Motor off

A calibration curve of the force in Newtons versus the force in permille is given in appendix figure B.11. This calibration data was used to determine the force delivered by the actuator in Newtons. Before the start of each measurement, a 'homing' command was used to reset the actuator. Also, each measurement was manually started about a second before the control scheme was activated. While the control scheme was active, the sensor's resistance was measured via four-terminal sensing by the SMU in an interval of approximately 230 milliseconds. A fixed current of $0.1 \mu\text{A}$ was delivered to the sensor by the SMU. The compliance voltage was set to 900 V. A script provided by Martijn Schouten made it possible to log the measurement data of the SMU. In each measurement, this script was manually activated a couple of seconds before the actuator's measurement was activated. This means that some zero-force data is present at the start of each resistance measurement. During measurements it was found that each sensor already had a resistance present in its original unfolded position. This is because the beam that connects the bottom and top plate, which was designed to be NinjaFlex, has PI-ETPU mixed in. While printing this beam, the 3D-printer's nozzles smeared a considerable amount of PI-ETPU into the beam. This happened in every single print. The additional resistance does not have to be a problem. This beam resistance is parallel to the contact resistance. So, ideally it would be larger than the contact resistance to have a larger sensing range. Figure 5.1 shows a representation of the electrical circuit of the sensor that is present with the new parallel beam resistance, R_p . In this circuit, switch $S1$ is supposed to close when the top and bottom plate make contact (when the threshold force is reached). The contact area resistance, R_a , changes as a function of applied load, W [N].

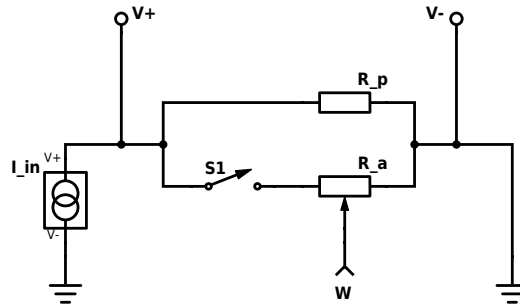


Figure 5.1: Schematic electrical representation of the sensor measurements

Given the presence of a parallel resistance, the model will have to be updated. When no force is applied, no contact resistance is present. Therefore, the measured resistance at zero force should be equal to the parallel resistance. Because some zero-force resistance is measured a couple of seconds before the actuator begins applying force, the maximum detected resistance in the first 30 resistance samples is taken to be equal to the parallel resistance, R_p . Then the model takes the minimum measured total resistance, $R_{t_{min}}$, which is expected to be equal to the resistance measured at maximum contact area. With the parallel resistance and minimum measured total resistance known, the minimum contact area resistance, $R_{a_{min}}$, can be determined with equation 5.1. This equation was derived from the parallel resistor equation $R_{t_{min}} = R_{a_{min}} // R_p$.

$$R_{a_{min}} = \frac{R_p \cdot R_{t_{min}}}{R_p - R_{t_{min}}} \quad (5.1)$$

Next, the peak force measured in the measurements is taken. At this peak force the contact area should be at its maximum, A_{max} (and the resistance at its minimum). Now the model can make a linear prediction of the contact resistance, R_a , versus contact area, A , with equation 5.2. The contact area is still calculated as described in section 4.2.

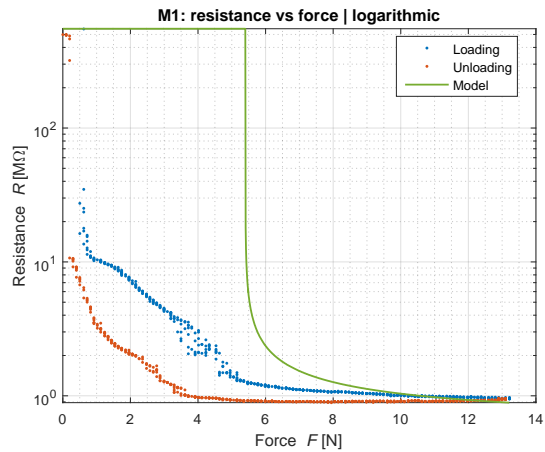
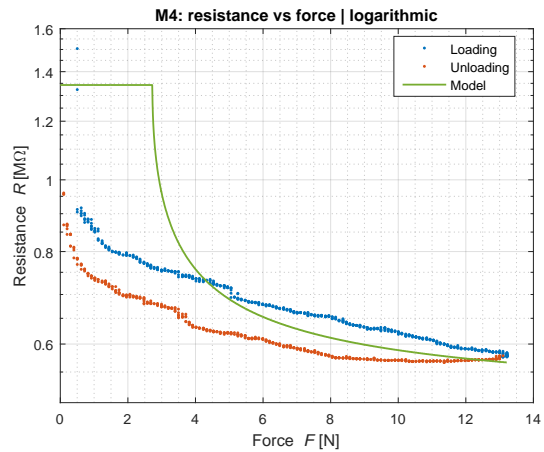
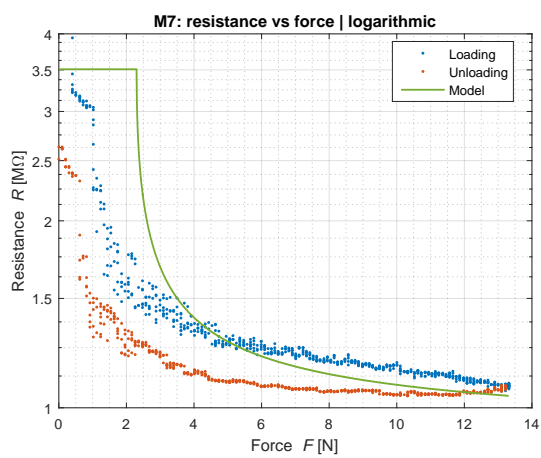
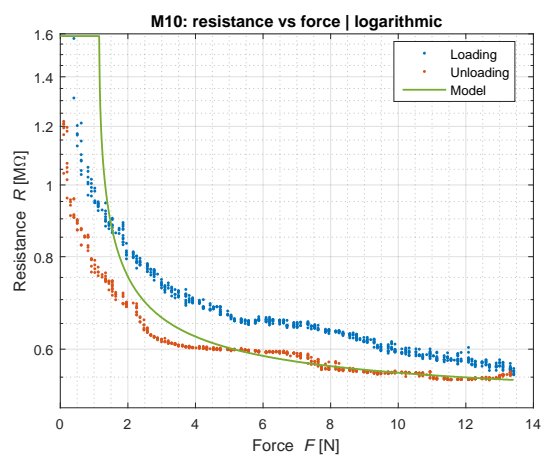
$$R_a(A) = \frac{A_{max}}{A} \cdot R_{amin} \quad (5.2)$$

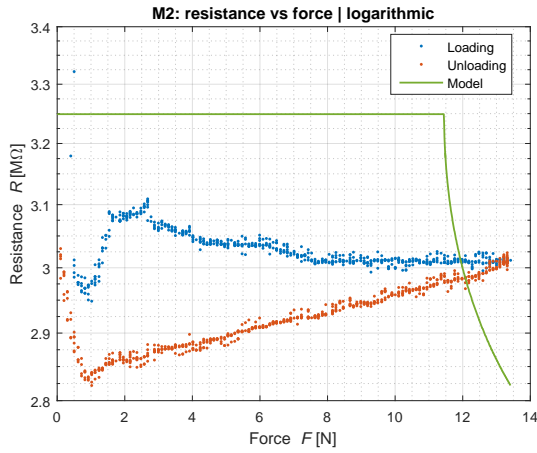
With the contact area resistance known, the total resistance, R_{model} , can be predicted with equation 5.3.

$$R_{model}(A) = \begin{cases} \frac{R_p \cdot R_a(A)}{R_p + R_a(A)}, & \text{if } A > 0 \\ R_p, & \text{otherwise} \end{cases} \quad (5.3)$$

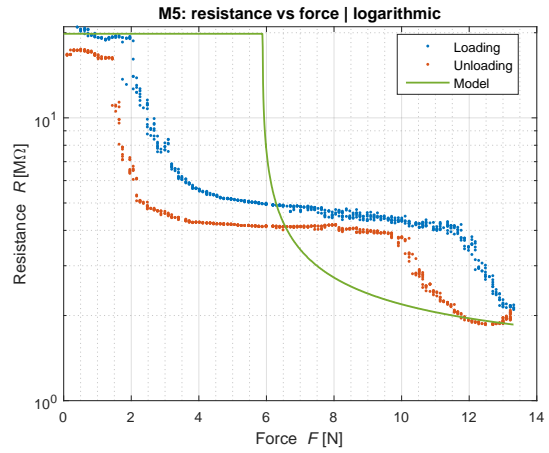
5.3 Measurements

The original displacement, force (converted to Newtons) and resistance measurements of the 12 sensors are shown in appendix figures B.12, B.13 and B.14. Because the measurements were manually started, each measurement has a different time offset between the displacement/-force data and the resistance data. This offset has been manually read per measurement by looking at identifiable changes that should occur at the same instance in time. An attempt was made to make a MATLAB script that could automatically identify this offset based on changes in derivatives, but proved not to be reliable (especially with sensors that did not make contact). Due to a lack of time, only the data of the ramp gradually going up and down has been examined. The displacement data can be used to see when the actuator first touches the sensor, by finding the instant at which the actuator reduces speeding towards the sensor. This way, the data recorded before the sensor was touched and after it was released was excluded. Next, the force and resistance data were aligned by rounding their time axis to 1 digit and checking at which points the rounded times were equal. This method was used as a quick fix to save time and should have ideally been replaced by a more accurate method, like interpolation. Loading of the sensor is considered up until the final moment the maximum force is reached and all following measurements are considered to represent unloading. The resulting measurements, together with the model predictions are shown in figures 5.2 for sensor size A, figure 5.3 for sensor size B and figure 5.4 for sensor size C. Mind that section 4.3 and table 4.2 describe what these size labels indicate. The vertical axis in the plots is logarithmic. In each measurement, a visual inspection was conducted to see if the top and bottom plate of the sensor actually made contact at any point in time. Table 5.2 indicates per sensor whether contact was made during the measurement. The table shows that sensors with smaller heights and larger lengths and widths require less force to make contact.

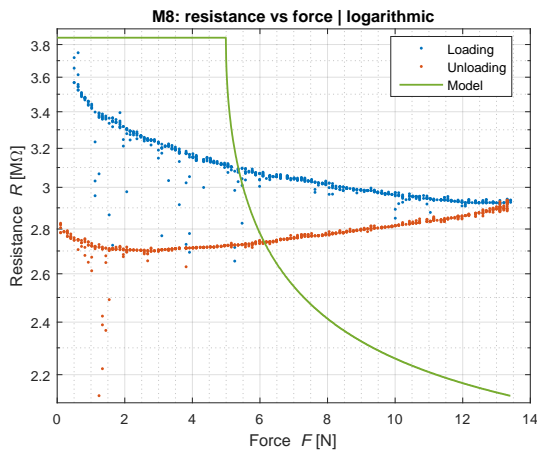
(a) Sensor A1: $h_1 = 0.8$ mm, $h_s = 0.4$ mm(b) Sensor A2: $h_1 = 0.8$ mm, $h_s = 0.2$ mm(c) Sensor A3: $h_1 = 0.6$ mm, $h_s = 0.4$ mm(d) Sensor A4: $h_1 = 0.6$ mm, $h_s = 0.2$ mm**Figure 5.2:** Resistance versus force measured and modeled for sensors with size label A: $L_1 = 10$ mm



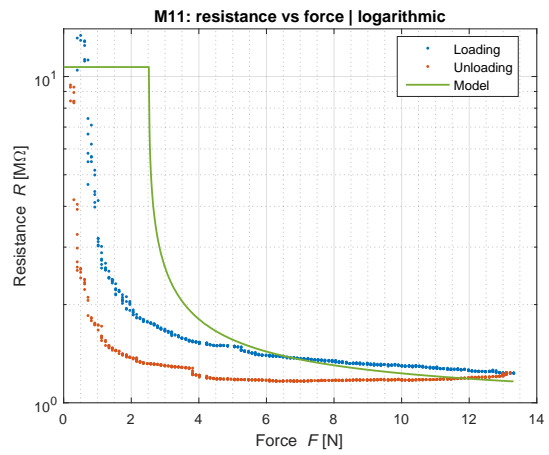
(a) Sensor B1: $h_1 = 0.8$ mm, $h_s = 0.4$ mm



(b) Sensor B2: $h_1 = 0.8$ mm, $h_s = 0.2$ mm



(c) Sensor B3: $h_1 = 0.6$ mm, $h_s = 0.4$ mm



(d) Sensor B4: $h_1 = 0.6$ mm, $h_s = 0.2$ mm

Figure 5.3: Resistance versus force measured and modeled for sensors with size label B: $L_1 = 7.5$ mm

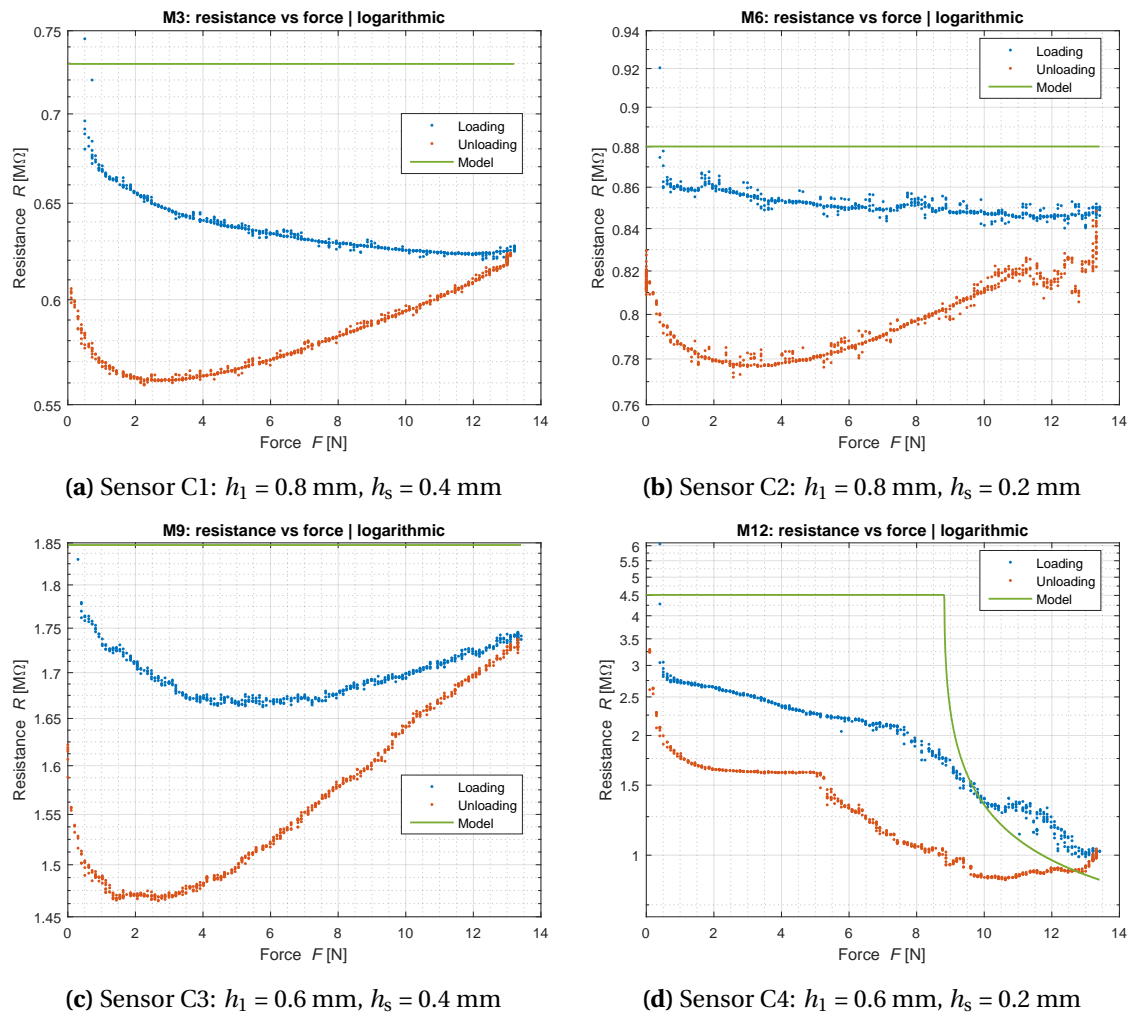


Figure 5.4: Resistance versus force measured and modeled for sensors with size label C: $L_1 = 5$ mm

Table 5.2: Indication whether a sensor made contact during the measurement based on visual inspection

Sensor	Contact?
A1	Yes
A2	Yes
A3	Yes
A4	Yes
B1	No
B2	Yes
B3	No
B4	Yes
C1	No
C2	No
C3	No
C4	Yes

Additionally, measurements with different source currents were conducted on sensor A1 to see if this would produce a different resistance readout and to see if the data is reproducible. The compliance voltage is kept at 900 V. The original data is shown in figure B.15 and the resistance versus force curves are shown in figure 5.5. Sourcing these different currents required voltages of up to 280 V (for 10 μ A) at high resistance values.

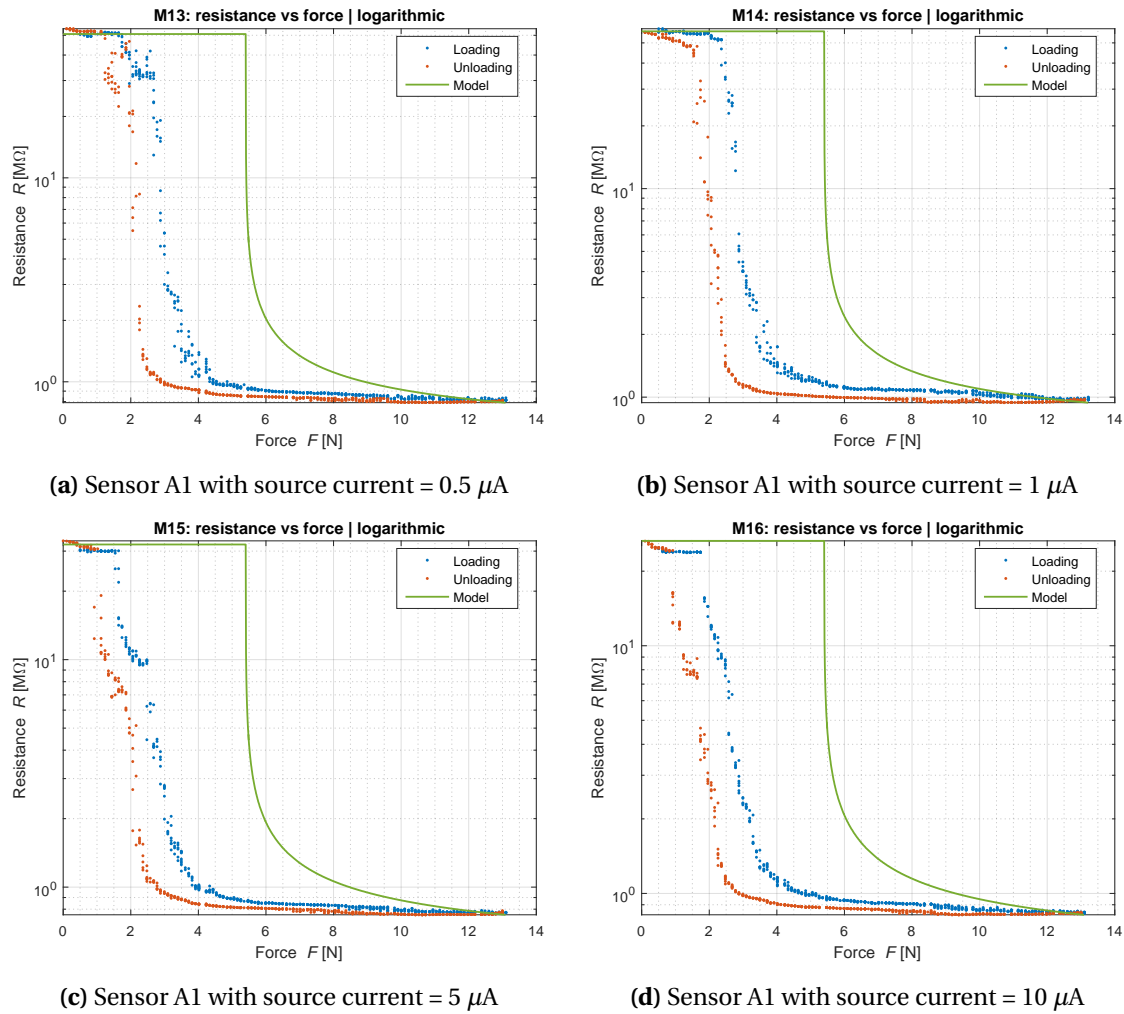


Figure 5.5: Resistance versus force measured and modeled for different source currents delivered to sensor A1: $L_1 = 10$ mm, $h_1 = 0.8$ mm, $h_s = 0.4$ mm

From the results shown in figures 5.2a, 5.5, B.12a and B.15 some observations were made. For a source current of $0.1 \mu\text{A}$, $0.5 \mu\text{A}$, $1 \mu\text{A}$, $5 \mu\text{A}$ and $10 \mu\text{A}$, the initial resistances (maximum resistance detected in the in first 30 data points of the unedited resistance measurements) are 551.6 M Ω , 50.7 M Ω , 56.8 M Ω , 32.1 M Ω and 26.5 M Ω , respectively. Furthermore, the resistance at peak force for $0.1 \mu\text{A}$, $0.5 \mu\text{A}$, $1 \mu\text{A}$, $5 \mu\text{A}$ and $10 \mu\text{A}$ are approximately 0.96 M Ω , 0.81 M Ω , 0.99 M Ω , 0.77 M Ω and 0.83 M Ω , respectively.

5.4 Discussion

The manual readout and compensation of time offsets is likely to be not fully accurate; it may deviate a couple of milliseconds and at most one second. This would not have been a problem if the measurement setup performed all measurements (i.e. distance, force and resistance) on the same time instances. Furthermore, the method that was used to align force and resistance data by rounding time data is crude and could have been replaced by a different method, like interpolation. The exclusion of the first seconds of each measurement was done to enable a comparison with the deflection. Unfortunately, this comparison has not been made due to a lack of time. For the comparison between force and resistance, however, these first seconds with zero force would have been useful and should not have been excluded in the loading part of the force/resistance measurement plots. Also, because the model does make use of these first seconds to determine the parallel resistance.

The measurement results of the sensors with label A in figure 5.2, show promising results in the sense that, from the moment the threshold force is reached, a gradual change in resistance is measurable in all cases. The model is accurate in that it correctly predicts that all four sensors make contact. However, the force at which the initial contact is made is predicted to be larger than it is in practice. Also, the drop in resistance is predicted to be more extreme than it is in practice in sensors A2, A3 and A4, but the contrary is true in sensor A1. The measurements on sensor A1 are not in line with the measurements on the other A-sensors; its zero-force resistance is over a hundredfold higher compared to all other sensors (B and C included). This is because the NinjaFlex beam that connects the bottom and top plate has little PI-ETPU smeared in it, significantly increasing the parallel resistance.

Of the B-sensors only sensors B2 and B4 had contact between the bottom and top plate, whereas the model predicted contact in all four sensors. It is interesting to see that even though sensors B1 and B3 have not made contact, their resistance does change depending on the load being applied to them. The resistances measured at start and end of sensor B1 do seem to approach each other. While loading, there are no significant changes in the resistance for sensor B1, but while unloading the resistance linearly decreases. This could be some strain-gauge effects in the parallel resistance, the beam that connects the bottom and top plate. Or perhaps the spacers show some resistance, because they too have a little bit of PI-ETPU smeared in. The shape of the measurement of B3 is different from the shape of B1 and sensor B3 experiences larger changes in resistance than sensor B1 does. This makes sense, because the height of the top and bottom plate of sensor B3 are smaller than those of sensor B1, so sensor B3 will experience larger physical deformations due to the applied forces. The model seems to hold up best with the measurement of sensor B4. Again, the sensor predicts too large of a force required for initial contact and when it does predict a contact, its decrease is more extreme than the measurements show. The measurements on sensor B2 show some interesting behaviour. A distinct platform (more or less constant high resistance) for forces up to 2 Newton is present, which has yet only mildly been seen in sensor A3. This may also have been more visible in other sensors if the first seconds of zero-force data would not have been excluded from the shown results. The model also shows this platform, which is expected to be present if no contact is made yet, for all sensors. Looking at loading, between 2 to 12 Newtons a decrease in resistance occurs. This is where first contact is made. Then another drastic decrease in resistance occurs after 12 Newtons. This behaviour is repeated during unloading, albeit at different forces. If we look at the unedited data in appendix figure B.13b, we too see this behaviour at the staircase measurement, so it is not some weird measurement artefact. Somewhere in the sensor extra contact area appears. A visual inspection of the sensor itself reveals two possible culprits. Referring to the point of view in figure 4.4, the top spacer of sensor B2 has a lot of PI-ETPU mixed in on its left side and so does the right side of the belt up to its second hole. When enough force is applied, it could be possible that additional contact is being made through the spacer or via the belt. The belt could be conducting the outer end of the bottom plate or the beginning of the rod, because over there the rod is pushed through the first hole in the belt and both the rod and belt have PI-ETPU mixed in around their connection with the PI-ETPU plates.

The measurements on sensors C1, C2 and C3 show similar results to B3. No big changes in resistance are present here, because these sensors do not make contact. The model is accurate on that (not making contact) as well. There are, however, some small force dependent resistance changes. These could be a combination of strain-gauge and hysteresis effects, or contact area effects due to PI-ETPU that has been smeared into the spacers. The model is also accurate in predicting that sensor C4 does make contact, which it does.

In general, nearly all sensors experience a drop in resistance at initial impact, including

the ones that do not make contact. This can be seen from initial resistance magnitude in the model, which is equal to the maximum measured resistance in the first 30 data points of the unedited resistance measurements. This could indicate that each sensor already has some contact area present somewhere, that increases from the beginning the actuator starts pushing. It is likely that this contact area is present in the NinjaFlex spacers, because they have PI-ETPU smeared in. In that case, one would expect this effect to be more clearly visible in the sensors with just a single layer of NinjaFlex to act as a spacer (0.2 mm) and that may be the case with sensor B2. It may also contribute to the seemingly more linear response of sensors A2 and C4, compared to their counterparts with a larger height.

Hysteresis is clearly present in all sensors. In none of the measurements was the lowest resistance value reached at maximum force, which is what the model did predict for all sensors that made contact. If we look at the unedited data in appendix figures B.12, B.13 and B.14, we see that for the sensors that do make contact, the lowest value in resistance is generally reached at the maximum step (force) in the staircase. So, assuming that the contact area is not increasing during unloading, the further decrease in resistance must have a different cause. It is likely that this is due to some strain-gauge-like effects as was discussed. These effects do not only have to be present in the connecting beam between the top and bottom plate, but can also be present in the top and bottom plates itself while they are still in contact. Additionally, surface conduction could also be playing a role here. Perhaps some high-pass filtering could be applied to compensate for the hysteresis and other drifts. This would, however, eliminate the possibility to measure static forces.

Something else that is visible in the measurements is the spread of resistance points per force step. This is (partly) because the resolution of the force measurements was 0.1 N and the deviation from the mean value was continuously switching between +0.1 N and -0.1N. It must be noted that these measurements did not exceed 14 Newtons, which is approximately equal to 1.4 kg. The forces exerted on a fingertip could exceed loads like these. If higher forces would have been measured, all sensors would eventually have experienced a decrease in resistance due to an increase in contact area. Which sensor is most useful would then depend on the application in which it is required. The sensors with smaller spacer and plate heights and larger plate lengths and widths have a lower threshold force and will be more force sensitive for smaller forces. Sensors with larger heights and smaller lengths and widths have a higher threshold force and will probably be more sensitive for larger forces. The height, length and width of the top and bottom plate determine the stiffness of the sensor. Less material, i.e. smaller height, length and width, equals less stiffness. The height of the spacers determine the amount of deflection required to make first contact, a lower height contributes to a lower threshold force.

For the sensors that did make contact, the model predicted a more extreme resistance decrease, because it does not consider the actual touching of the top and bottom plate. If this would be considered, the model would likely display a curve with a shape more similar to the measurements. More on this problem was already discussed in chapter 4. Furthermore, the model does not take into account hysteresis. Also, the model's initial resistance is higher in all measurements, as is already explained above.

Another deviation results from the fact that the model assumes a uniform load. From the picture in appendix figure B.10, it can be seen that the actuator's tip, which is in contact with the sensor, is smaller than the sensor that is being tested (which is a sensor of size A in that picture). Furthermore, the tip is of a solid, non-compressible plastic. It will not apply a uniform load the way is considered in the model, i.e. a load that remains uniform under plate

deflection. Especially so for sensor types B and C, where the tip is larger than the sensors and could be modelled as a flat plate pushing the sensor.

Another thing to note is the observations made in chapter 3, where it was found that specified dimensions are not necessarily equal to the dimensions that are actually 3D-printed. It is highly probable that the specified dimensions, which were used in the model, do not equal the dimensions present in practice. Yet another reason for deviations are the Young's moduli that have been assumed. These are based on the average absolute Young's moduli found in chapter 3, which may not be sufficiently accurate for the sensor.

The plots with different source currents shown in figure 5.5, look very similar in shape, indicating that the data is reproducible for the same sensor. The magnitudes of the resistance measurements are not equal, however, for large resistance values. This shows that the source current, I_{IN} in figure 4.4, does make a difference on the resistance measurements. As was stated in section 5.3, a source voltage of up to 280 V was required to keep a $10 \mu\text{A}$ source current at high resistance. A voltage this high affects the measurements, because the contact plates are very close to each other, resulting in unreliable measurements for high resistances. The maximum voltage of 280 V in combination with a current of $10 \mu\text{A}$ means that a maximum power of $280 \times 10 \cdot 10^{-6} = 2.8 \text{ mW}$ is being dissipated in the sensor. Even though this power is not high and not continuously applied to the sensor, resistive sensor generally suffer from thermal effects. So, the power dissipation may play a role in differences obtained during the measurements. Also in the decreasing resistance during unloading, because power has then been applied for a longer time, possibly heating up the sensor. These possible problems induced by high voltage levels are also why the lowest possible source current, $0.1 \mu\text{A}$, was used in the other measurements, to keep the source voltage as low as possible. Except for sensor A1, where the source voltage reached 50 V, the source voltage was kept below 2 V in the regular measurements. That a low source voltage does yield similar resistance measurements for different source currents, can be seen in the resistances measured at peak force. Herein, where the resistance is relatively low and the source current does not require a large source voltage, no clear pattern is visible in the deviations in measured resistance for different source currents.

5.5 Conclusion

In this chapter, characterization of the sensor design was elaborated upon. All twelve sensors were measured on their resistance-force characteristics. It was found that a smaller height and larger length and width contribute to a lower threshold force for initial contact between the bottom and top plate. Some of the sensors with larger height and smaller length and width did not experience a contact point between the bottom and top plate in the range of forces that they have been tested in, because they have a higher threshold force. The sensors that did make contact are more sensitive to small forces than the ones that did not, because their dimensions make that they are less stiff. It would be interesting to do measurements with larger forces. In the measurement results, some unexpected resistance changes were observed that are likely due to PI-ETPU being present at places where only NinjaFlex should be present. Also, hysteresis has been found to play a big role in the measurements. Filtering could possibly be applied to compensate for this. Furthermore, it was found that the source current influences the resistance measurements for high resistances. The source current should be kept as low as possible to prevent high voltages being required, which could affect the measurements thermally. The model was found to be accurate in predicting which sensors would experience contact between the bottom and top plate. However, in all of those cases a too high force was modelled to coincide with the first point of contact and a too steep decline in resistance was modelled. The model is not fully accurate and could do with some improvements. The results discussed in this chapter can form the basis for these improvements.

6 Conclusion and Recommendations

6.1 Conclusion

In the research conducted for this bachelor's thesis, a flexible fingertip strain sensor was designed and characterized. This sensor was 3D-printed from NinjaFlex and PI-ETPU and can measure the normal force acting on a fingertip. Conclusions drawn from the research on this sensor are listed below.

- This research has shown that FSR sensors can be made from 3D-printed structures with an area down to 25 mm^2 and a height in the order of millimeters.
- Multi-material 3D-printing on a small scale has shown to be difficult, with materials being mixed together where they should not be mixed together. Printing TPU in arbitrary orientations has been proven problematic as well. Using other printing equipment and/or supporting material could be beneficial here.
- The datasheet provided by the manufacturer of PI-ETPU 95-250 Carbon Black contains information on the Young's modulus and resistivity that has not been reproducible during this research.
- A model has been introduced that has given some qualitative understanding of the FSR operation. It is not sufficiently accurate in follow the resistance-force response of the sensors and could be improved on the following points:
 - Modelling the deformations of the bottom plate. At the moment, the bottom plate is assumed to be flat and rigid.
 - A better description of the possible loading conditions. The model currently only assumes homogeneous loading.
 - The current deflection and compression equations may not hold true for the magnitude of plate deflections and compressions that are present in the sensor.
 - The assumptions made in general should be more physically realistic.
- Resistance changes are currently generally in the range of $500 \text{ k}\Omega$ to $4 \text{ M}\Omega$ with a couple of exceptions. Ideally, this would be reduced to values only in the order of $\text{k}\Omega$'s for less power consumption and easier electronic readout.
- Hysteresis has shown to have a significant effect on the measurements. Thermal effects could be present too. Signal filtering may be helpful here.

Two of the goals listed in the introduction have not been reached in this research. Producing a sensor that does not require an assembly has not been achieved and no research was conducted on how and if shear forces could be measured as well. All other goals that were set for this research have been reached.

6.2 Recommendations

The work conducted in this research was a first step towards making a 3D-printed flexible fingertip strain sensor. Some recommendations are listed below in case work on this topic is proceeded.

- The most important recommendation is that the sensor model needs a complete re-design for it to be useful and create a good understanding of the working principles of the sensor. The assumption of a uniform load may not hold true, the beam equations it is based on may not hold true for the designed sensor and the model should account for the change in physical behaviour of the sensor when the bottom and top plates come into contact.
- Analysis of the measurements on the Young's modulus was rushed as it had already taken a lot of time. Instead of simply taking average values, one could have a better look at what the actual Young's modulus applicable to the sensor is.
- Measurements were only conducted up to about 13.5 Newtons. It would be interesting to see how the sensors perform at larger forces.
- Signal filtering could be researched to obtain better results.
- Twelve sensors with different dimensions were made for comparison. It needs to be determined which sensor dimensions yield the best results (also depends on the intended application). The goal of making the sensor as small as possible should be kept in mind here.
- A foldable design was turned to, because printing a small sensor with two stacked plates failed. This is due to limitations of the printer and difficulties of the material (PI-ETPU) being printed. One could have a look at printers with a higher resolution, better extrusion control, smaller nozzles, or other available conductive TPU's that may be better printable. Also, the option of using supporting material could be looked at. This could be done with the current printing configuration, but then one of the TPU's would have to be switched with supporting material during printing. A printer with 3 nozzles would then be more easy.
- The current design requires an assembly. Other designs may be possible that do not require an assembly. This could be in combination with the other recommendation of looking for a better way to print the sensor. If work on the current design would be continued, the option of extending the design to which it holds two sensors could be reviewed. At the moment, there are two contact leads for electrical wires on the bottom side of the design. On the top side, however, there is space to print a contact beam that could be the extension to another FSR sensor. One sensor could then be measuring the fingertip and the other could be measuring another segment of the finger.
- The design was focussed on the FSR transduction principle. Perhaps a capacitive could have better results if the issue of requiring complex electronics could be overcome.
- Besides four-terminal sensing with an SMU, no other options of electronic readout have been examined. One could have a look into finding a configuration with a Wheatstone bridge, for example. Power consumption and portability will then have to be taken into account.

A Tables

Table A.1: Coefficients of the 4th order polynomial fits used in figure B.5b for NinjaFlex

Beam	Coefficient 1 ($\times 10^8$)	Coefficient 2 ($\times 10^8$)	Coefficient 3 ($\times 10^8$)	Coefficient 4 ($\times 10^6$)	Coefficient 5 ($\times 10^3$)
NinjaFlex 1mm, Horizontal	-96.71	21.6	-1.75	21.70	69.62
NinjaFlex 1mm, Vertical	-393.53	64.4	-3.64	22.46	45.09
NinjaFlex 2mm, Horizontal	-770.06	69.47	-2.6	21.47	31.25
NinjaFlex 2mm, Vertical	-169.20	15.52	-0.86	15.82	6.68
NinjaFlex 3mm, Horizontal	-469.88	44.33	-1.86	19.42	0.46
NinjaFlex 3mm, Vertical	-523.92	47.73	-1.95	15.33	95.25

Table A.2: Coefficients of the 4th order polynomial fits used in figure B.5d for PI-ETPU

Beam	Coefficient 1 ($\times 10^9$)	Coefficient 2 ($\times 10^9$)	Coefficient 3 ($\times 10^9$)	Coefficient 4 ($\times 10^6$)	Coefficient 5 ($\times 10^3$)
PI-ETPU 1mm, Horizontal	-406.84	36.69	-1.4	59.16	128.82
PI-ETPU 1mm, Vertical	-516.73	41.21	-1.41	57.31	38.47
PI-ETPU 2mm, Horizontal	-658.74	51.06	-1.69	62.70	112.77
PI-ETPU 2mm, Vertical	-544.41	49.08	-1.89	70.64	-94.47
PI-ETPU 3mm, Horizontal	-1406.64	83.51	-2.09	62.47	207.94
PI-ETPU 3mm, Vertical	-166.85	22.96	-1.29	67.39	-192.56

Table A.3: 3D-printer settings used during printing of the sensors. Printer: Flashforge Creator Pro 2016 with Flexion Extruder. Software: Simplify3D.

Setting	NinjaFlex	PI-ETPU
Extrusion multiplier	0.7	1.25
Extrusion width	0.55	0.7
Primary layer height	0.2 mm	0.2 mm
First layer height	200%	200%
Use skrit/brim	No	Yes 15 mm distance
Use ooze shield	Yes 12.5 mm distance	No
Infill	100% rectilinear	100% rectilinear
Temperature	220 °C	230 °C
Bed temperature	50 °C	50 °C
Cooling fan	Start at 2 nd layer 35% power	Start at 2 nd layer 35% power
Print speed	2000 mm/min	2000 mm/min

B Graphs

B.1 Young's Modulus

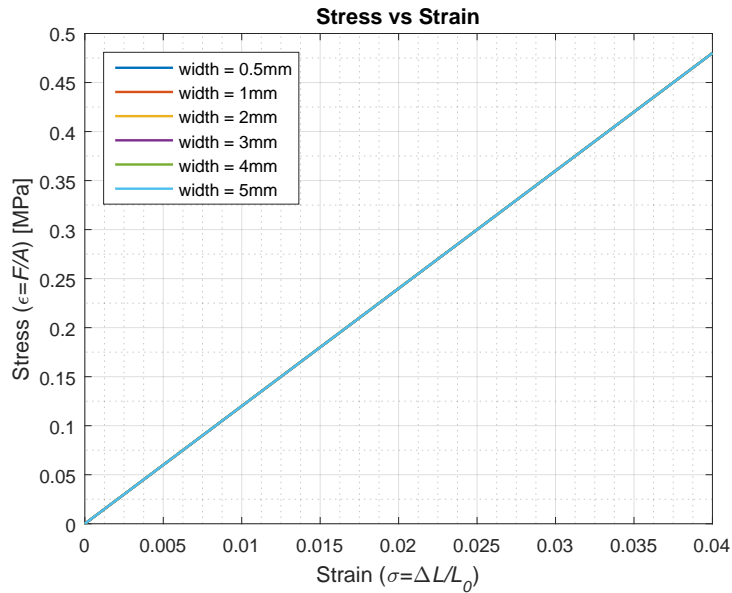


Figure B.1: Modeled stress vs strain for NinjaFlex and PI-ETPU structures with varying thicknesses (widths)

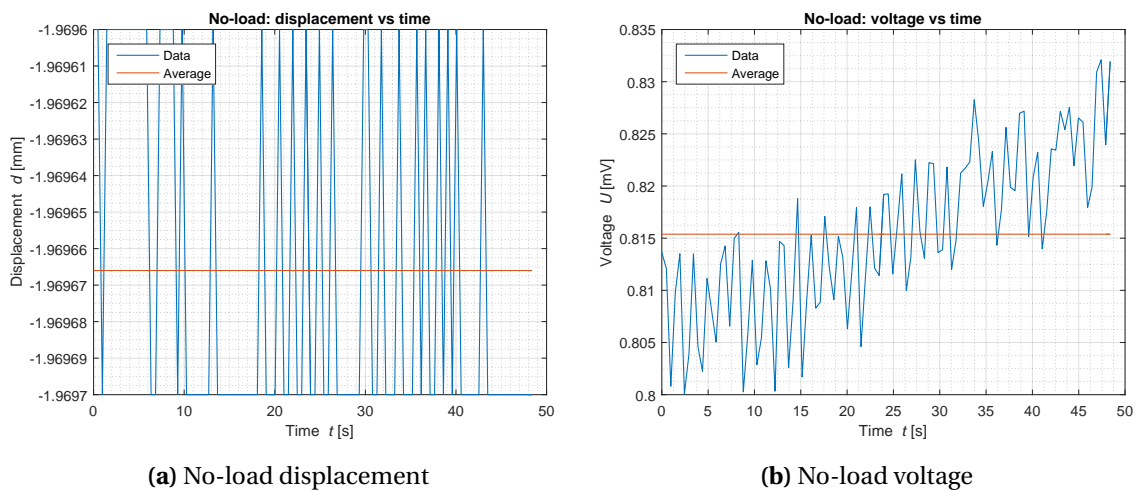
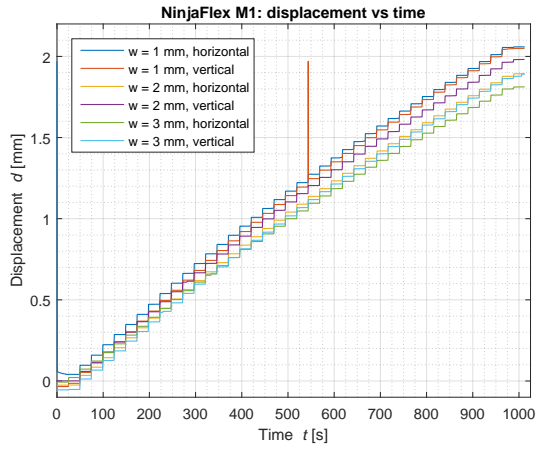
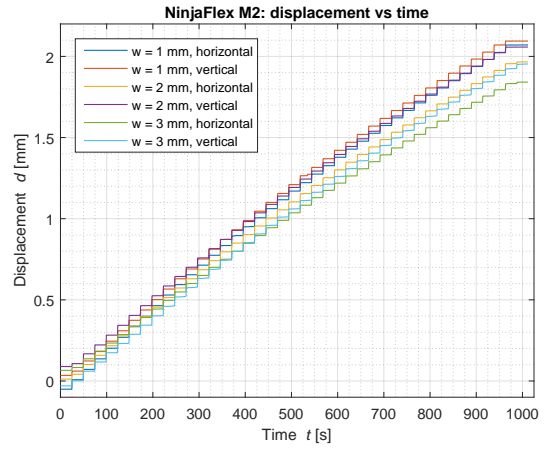


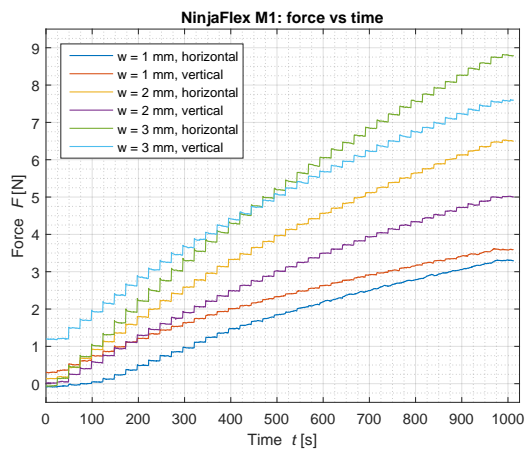
Figure B.2: No-load Young's modulus offset measurements: displacement and voltage over time for 6 different beams



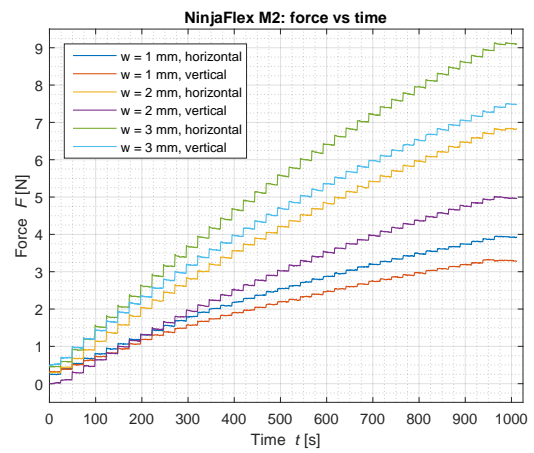
(a) NinjaFlex displacement measurement 1



(b) NinjaFlex displacement measurement 2

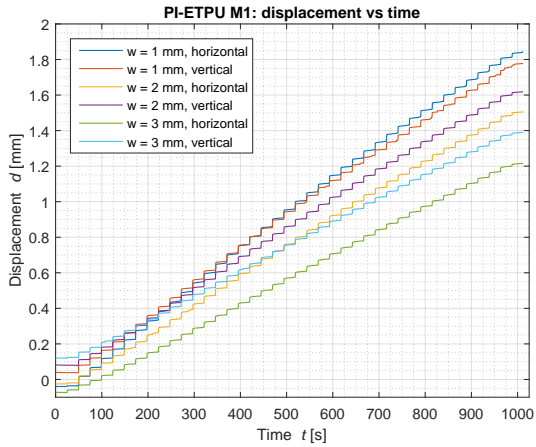


(c) NinjaFlex force measurement 1

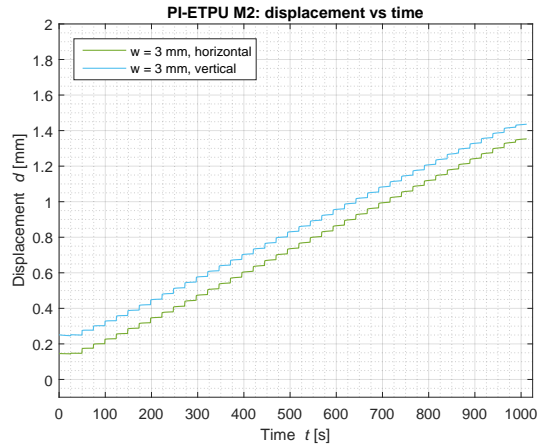


(d) NinjaFlex force measurement 2

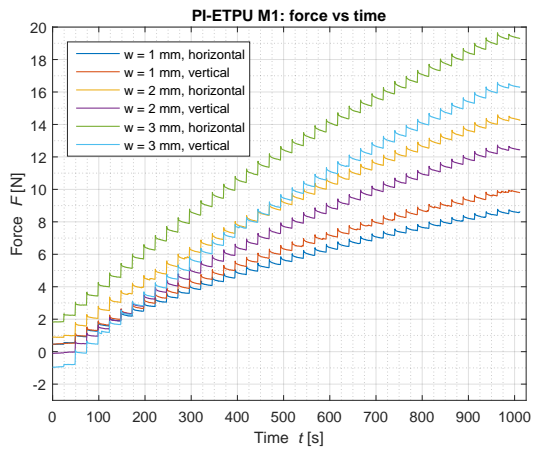
Figure B.3: NinjaFlex Young's modulus measurements: displacement and force over time for 6 different beams



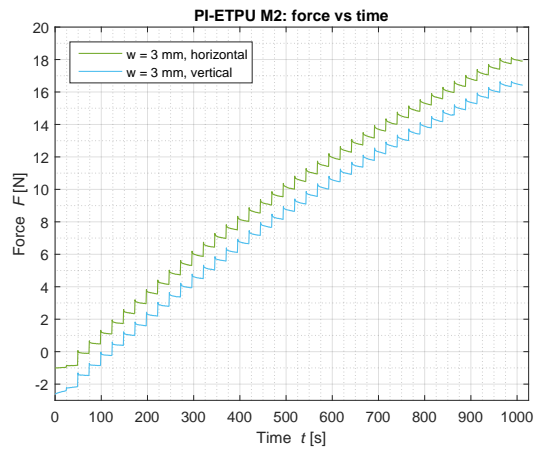
(a) PI-ETPU displacement measurement 1



(b) PI-ETPU displacement measurement 2

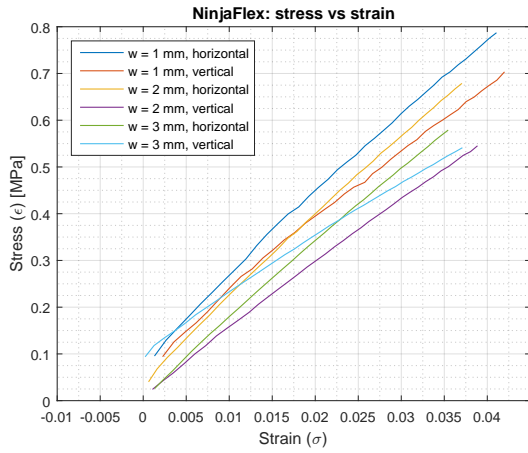


(c) PI-ETPU force measurement 1

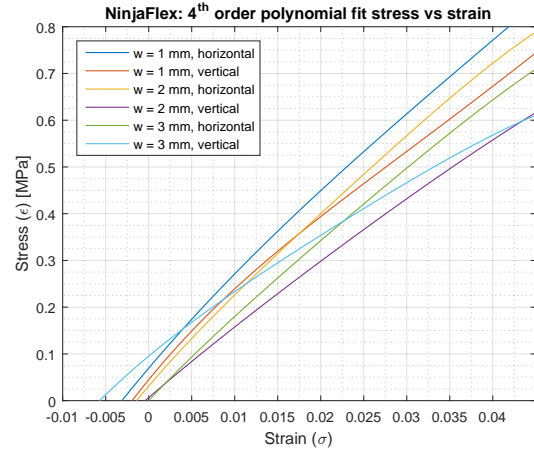


(d) PI-ETPU force measurement 2

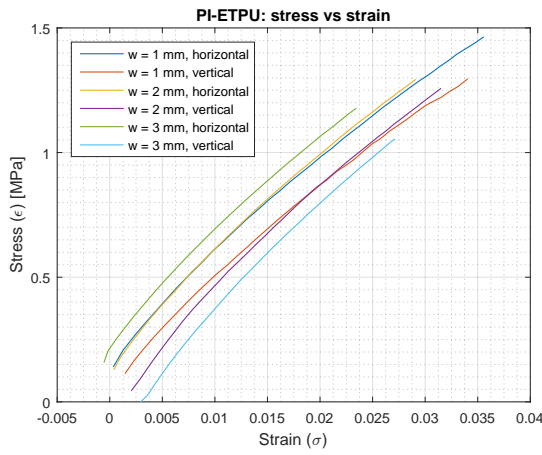
Figure B.4: PI-ETPU Young's modulus measurements: displacement and force over time for 6 different beams



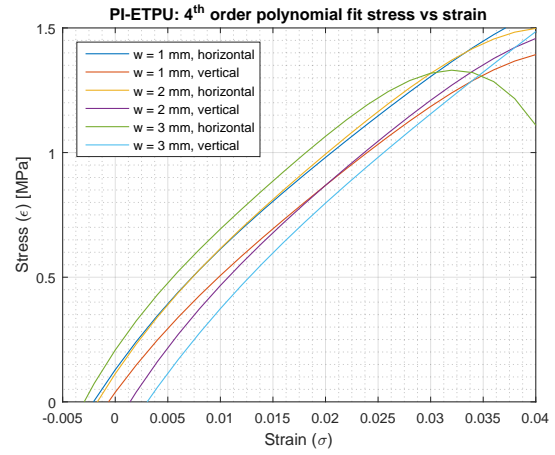
(a) NinjaFlex stress vs strain



(b) NinjaFlex 4th order polynomial fit stress vs strain

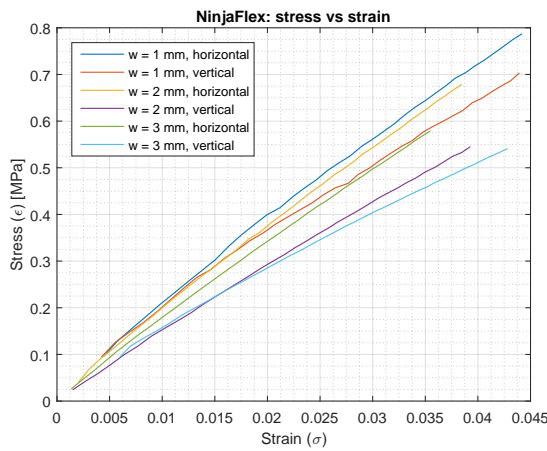


(c) PI-ETPU stress vs strain

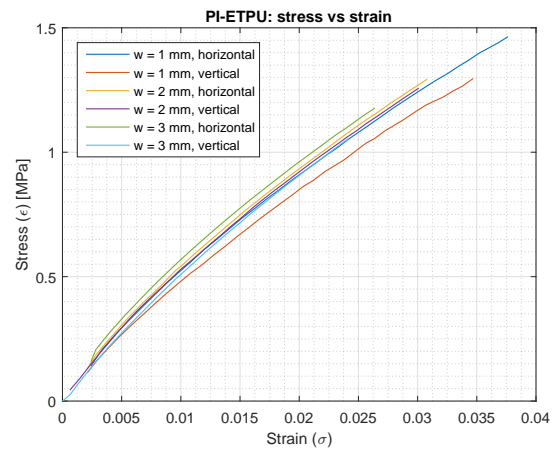


(d) PI-ETPU 4th order polynomial fit stress vs strain

Figure B.5: NinjaFlex and PI-ETPU intermediate stress vs strain and their 4th order polynomial fits for 6 different beams



(a) NinjaFlex stress vs strain



(b) PI-ETPU stress vs strain

Figure B.6: NinjaFlex and PI-ETPU final stress vs strain for 6 different beams

B.2 Sensor Modelling and Design

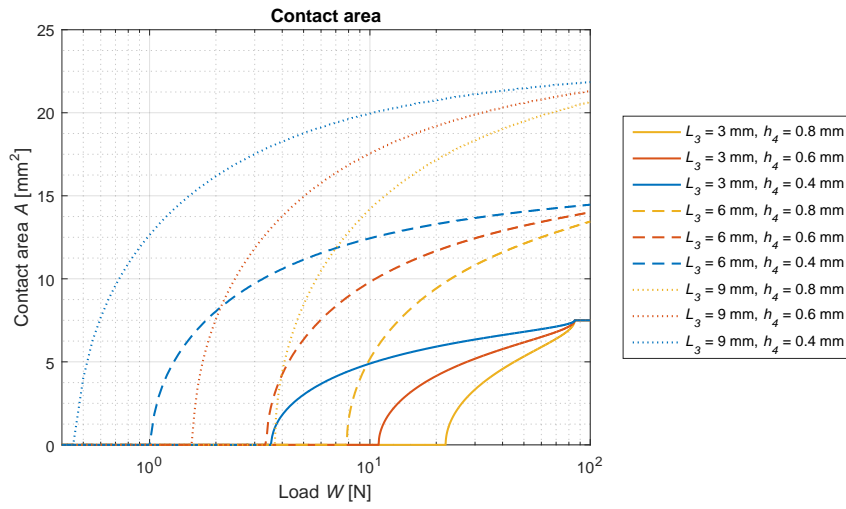


Figure B.7: Sensor model logarithmic plot of contact area versus applied load for various top plate lengths and heights

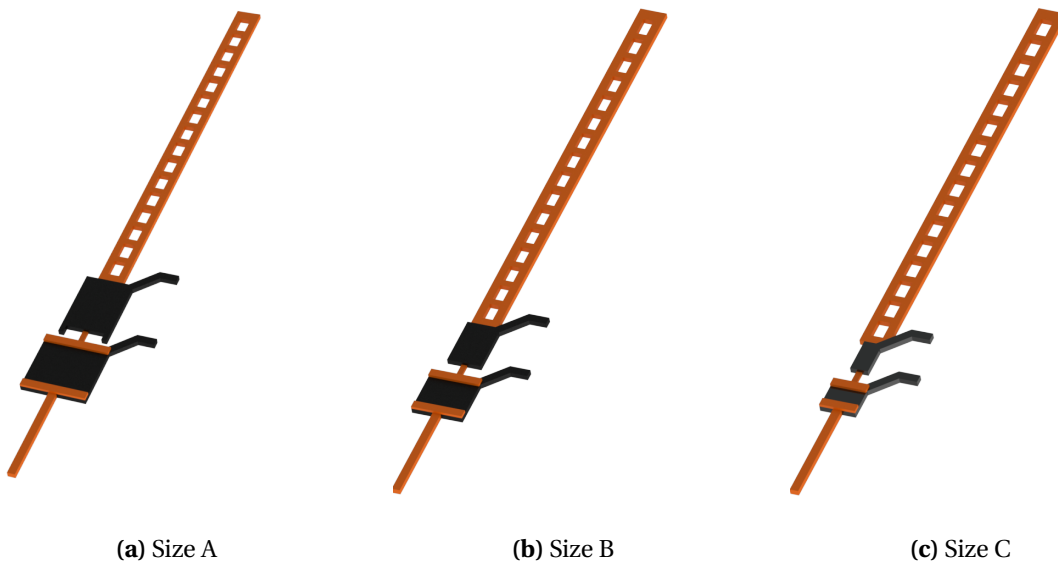


Figure B.8: Three different area sizes of the sensor design

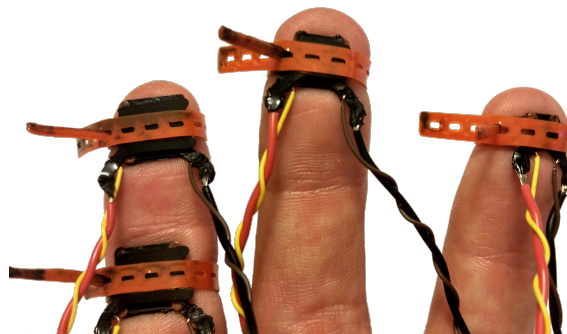


Figure B.9: Sensor placement on fingers. From left to right: size A, size B, size C.

B.3 Sensor Characterization

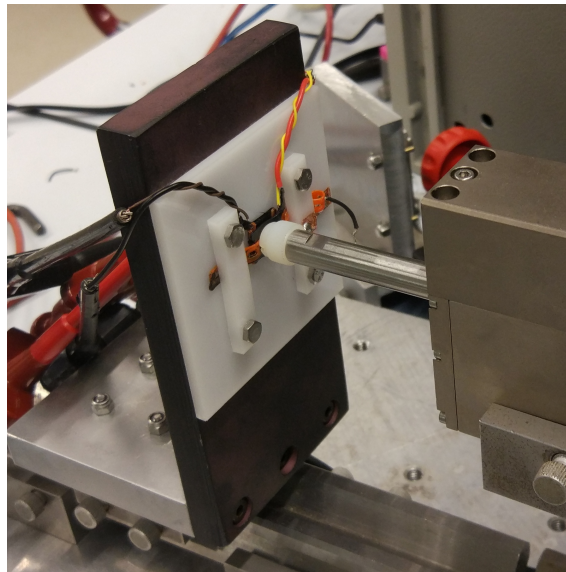


Figure B.10: Sensor measurement setup with SMAC actuator applying force to the sensor

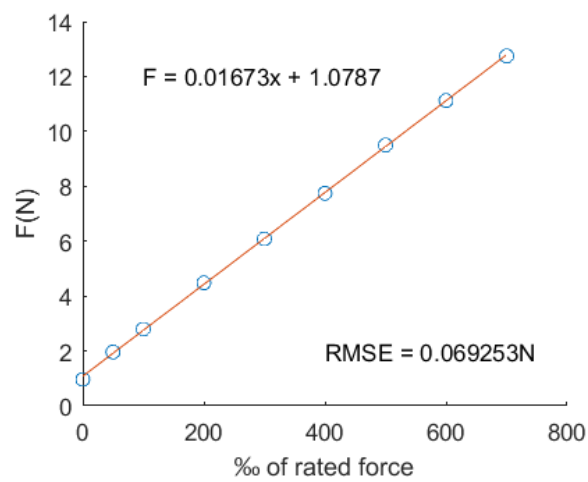


Figure B.11: SMAC actuator force calibration curve. This figure was provided by Martijn Schouten.

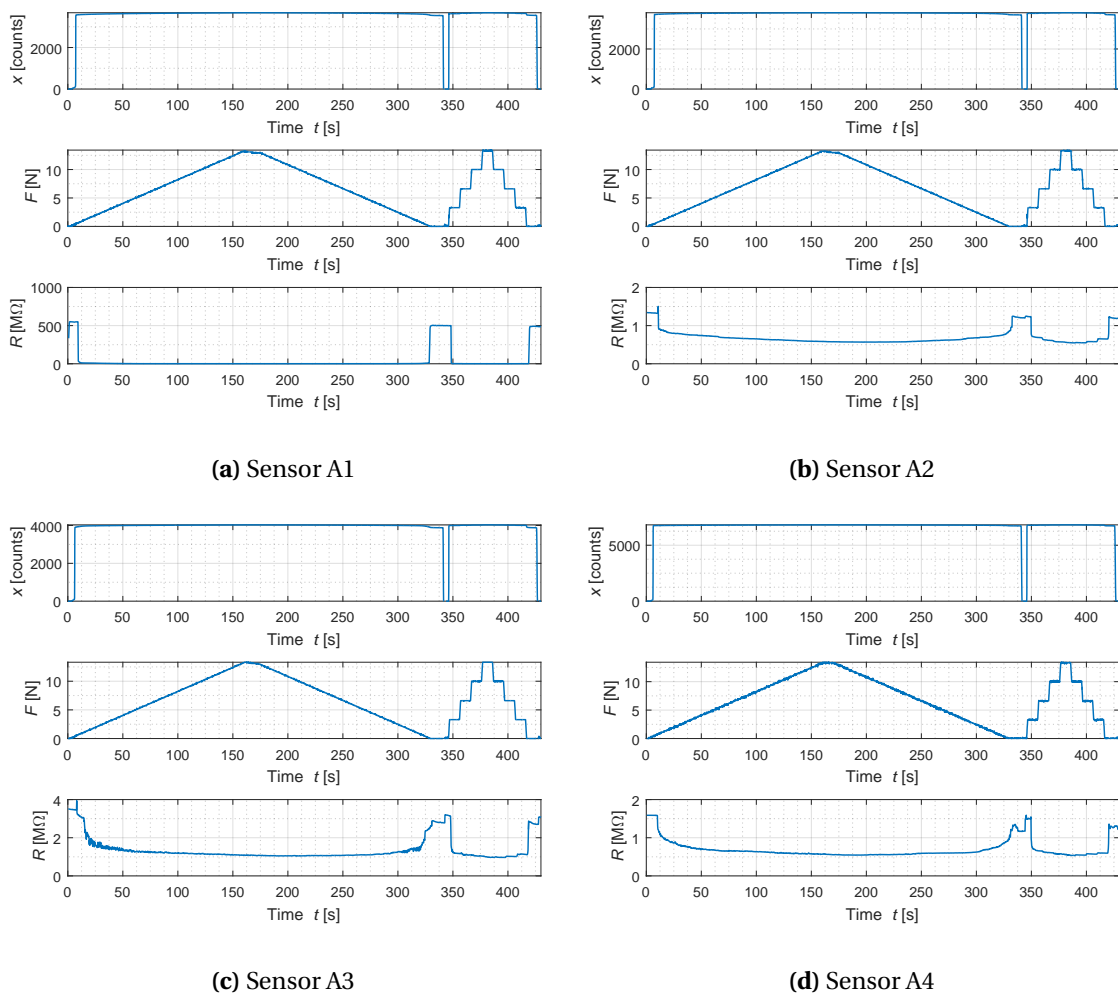


Figure B.12: Original displacement [counts], force [N] and resistance [$M\Omega$] measurement data of sensor size A

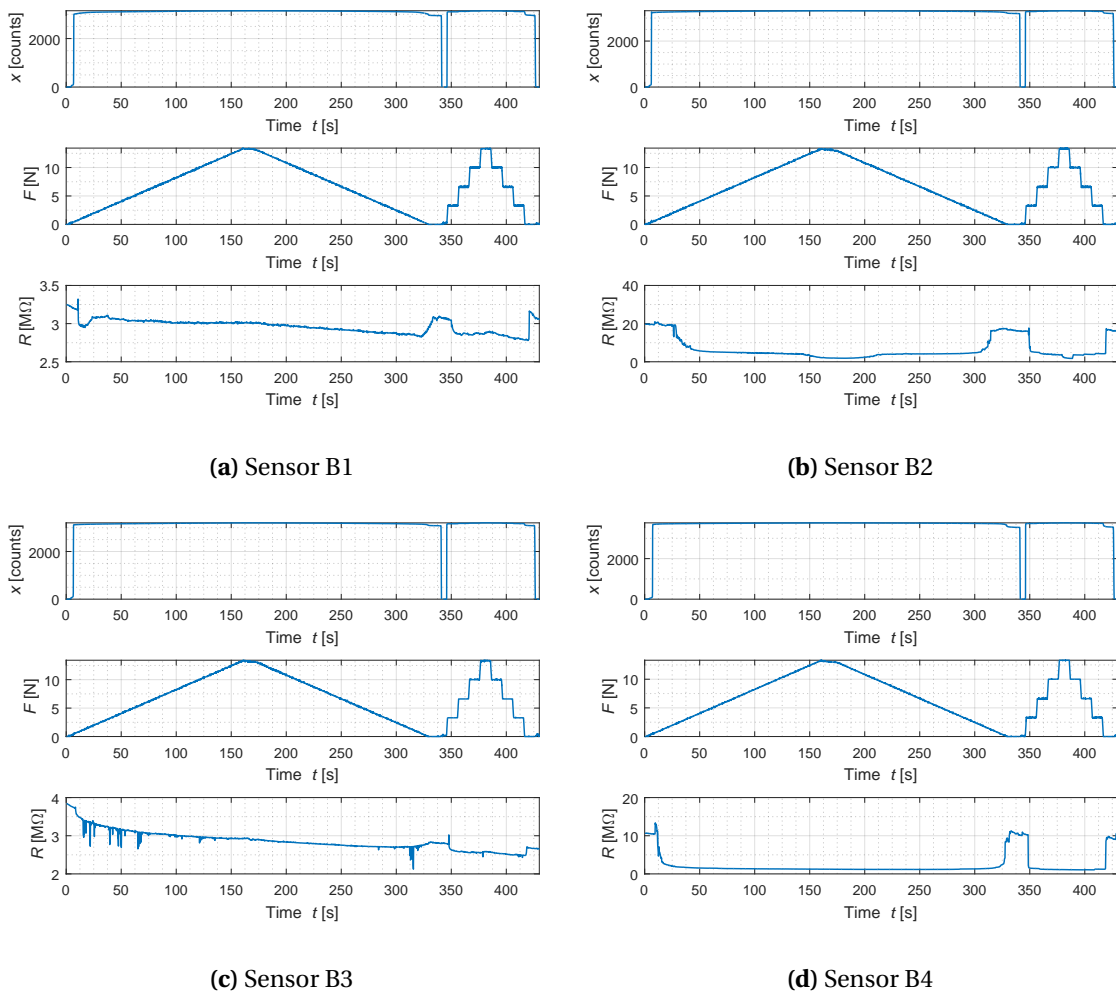


Figure B.13: Original displacement [counts], force [N] and resistance [M Ω] measurement data of sensor size B

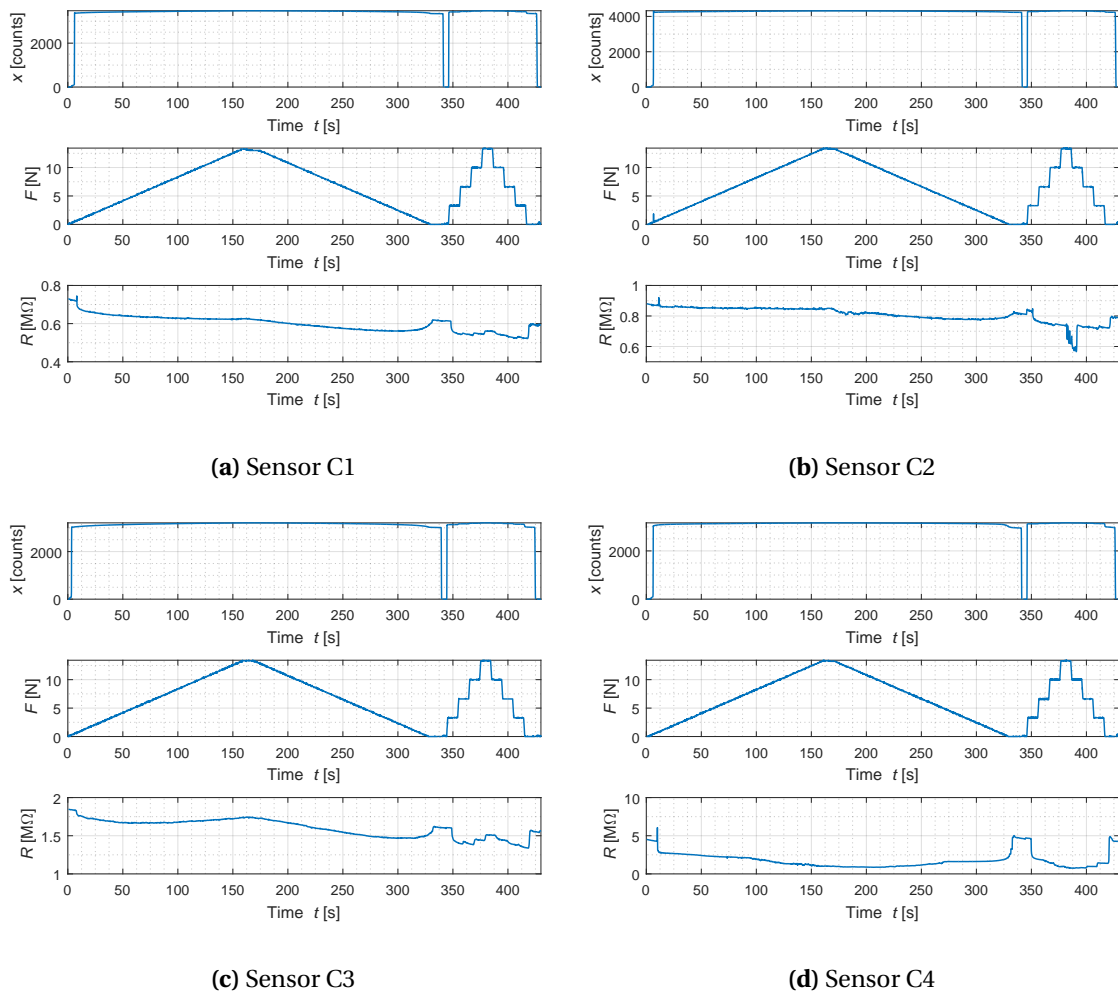


Figure B.14: Original displacement [counts], force [N] and resistance [$M\Omega$] measurement data of sensor size C

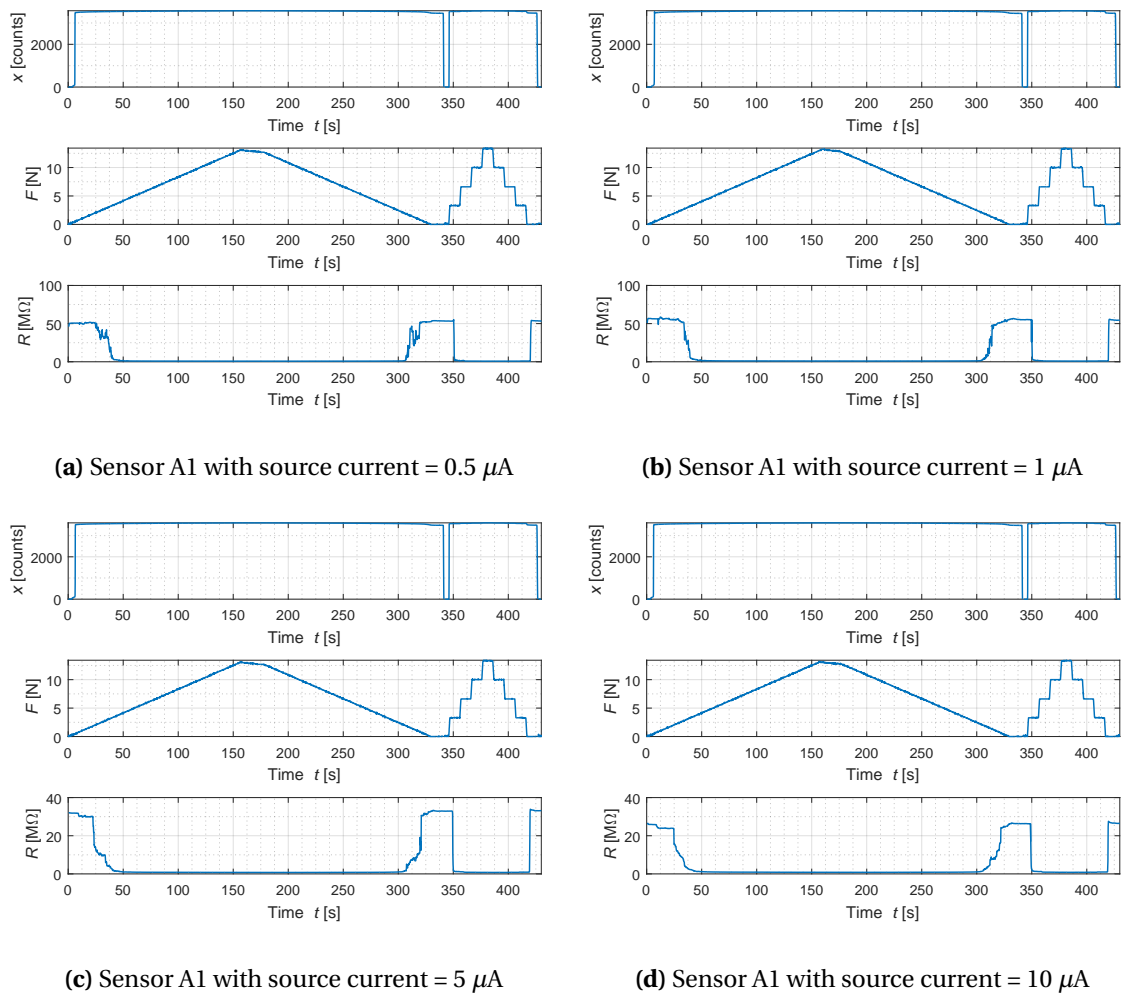


Figure B.15: Original displacement [counts], force [N] and resistance [$\text{M}\Omega$] measurement data for different source currents delivered to sensor A1

C Equations

$$R(d) = 4 \frac{5}{33} d \cdot 10^6 \quad (\text{C.1})$$

$$R_a(A) \approx -6.61A \cdot 10^{10} + 2.48 \cdot 10^8 \quad (\text{C.2})$$

$$R_b(A) \approx -8.29A \cdot 10^{10} + 2.72 \cdot 10^8 \quad (\text{C.3})$$

$$R_c(A) \approx -5.74A \cdot 10^{10} + 2.48 \cdot 10^8 \quad (\text{C.4})$$

$$R_d(A) \approx -7.27A \cdot 10^{10} + 2.70 \cdot 10^8 \quad (\text{C.5})$$

Bibliography

- [1] Amazing AM (2017), What is Additive Manufacturing?
<http://additivemanufacturing.com/basics/>
- [ASTM International] ASTM International (), Standard Test Method for Tensile Properties of Plastics.
<http://classes.engr.oregonstate.edu/mime/winter2012/me453-001/Lab1%20-%20Shear%20Strain%20on%20Polymer%20Beam/ASTM%20D638-02a.pdf>
- [3] Büscher, G. H., R. Kõiva, C. Schürmann, R. Haschke and H. J. Ritter (2015), Flexible and stretchable fabric-based tactile sensor, *Robotics and Autonomous Systems*, **vol. 63**, pp. 244 – 252, ISSN 0921-8890, doi:<http://dx.doi.org/10.1016/j.robot.2014.09.007>, advances in Tactile Sensing and Touch-based Human Robot Interaction.
<http://www.sciencedirect.com/science/article/pii/S0921889014001821/>
- [4] Chorley, C., C. Melhuish, T. Pipe and J. Rossiter (2009), Development of a tactile sensor based on biologically inspired edge encoding, in *2009 International Conference on Advanced Robotics*, IEEE, pp. 1–6.
<http://ieeexplore.ieee.org/document/5174720/>
- [CodeCogs] CodeCogs (), Built in Beams II.
<http://www.codecogs.com/library/engineering/materials/beams/built-in-beams-ii-.php>
- [CodeCogs] CodeCogs (), Simple Supported Beams.
<http://www.codecogs.com/library/engineering/materials/beams/simple-supported-beams.php>
- [7] Dahiya, R. S., G. Metta, M. Valle and G. Sandini (2010), Tactile Sensing #x2014;From Humans to Humanoids, in *IEEE Transactions on Robotics*, volume 26, IEEE, pp. 1–20, ISSN 1552-3098, doi:10.1109/TRO.2009.2033627.
<http://ieeexplore.ieee.org/document/5339133/>
- [8] Dahiya, R. S. and M. Valle (2013), *Tactile Sensing Technologies*, Springer Netherlands, Dordrecht, pp. 79–136, ISBN 978-94-007-0579-1, doi:10.1007/978-94-007-0579-1_5.
http://dx.doi.org/10.1007/978-94-007-0579-1_5
- [9] Drimus, A., V. Jankovics, M. Gorsic and S. Mátéfi-Tempfli (2014), Novel high resolution tactile robotic fingertips, in *IEEE SENSORS 2014 Proceedings*, IEEE, pp. 791–794, ISSN 1930-0395, doi:10.1109/ICSENS.2014.6985118.
<http://ieeexplore.ieee.org/document/6985118/>
- [10] Elleuch, R., K. Elleuch, B. Salah and H. Zahouani (2007), Tribological behavior of thermoplastic polyurethane elastomers, **vol. 28**, no.3, pp. 824 – 830, ISSN 0261-3069, doi:<http://dx.doi.org/10.1016/j.matdes.2005.11.004>.
<http://www.sciencedirect.com/science/article/pii/S0261306905003067>
- [11] Hammond, F. L., Y. Mengüç and R. J. Wood (2014), Toward a modular soft sensor-embedded glove for human hand motion and tactile pressure measurement, in *2014 IEEE/RSJ International Conference on Intelligent Robots and Systems*, pp. 4000–4007, ISSN 2153-0858, doi:10.1109/IROS.2014.6943125.
- [12] Interlink Electronics (2015), *FSR Integration Guide*.
http://www.interlinkelectronics.com/integration_guides/FSR400Series_IG.zip

- [MathWorks] MathWorks (), polyfit.
<https://www.mathworks.com/help/matlab/ref/polyfit.html>
- [14] MB Dynamics (1997), *PM-SHAKERS*.
<http://www.mbdynamics.com/PDF/PM-SERIES.pdf>
- [15] Miko Elwenspoek, Gijs Krijnen, R. W. T. L. (2015), *Introduction To Mechanics And Transducer Science*, chapter 6, pp. 107 – 118.
- [National Institute of Standards and Technology] National Institute of Standards and Technology (), standard acceleration of gravity.
<http://physics.nist.gov/cgi-bin/cuu/Value?gn>
- [NDT Resource Center] NDT Resource Center (), Anisotropy and Isotropy.
<https://www.nde-ed.org/EducationResources/CommunityCollege/Materials/Structure/anisotropy.htm>
- [18] NinjaTek (2016), *NinjaFlexö 3D Printing Filament*.
<https://ninjatek.com/wp-content/uploads/2016/05/NinjaFlex-TDS.pdf>
- [19] OpenTech (2013), Fused Deposit Modeling.
<https://www.opentech.tw/pages/documents/?/intro/C4-1.html>
- [20] Palmiga Innovation (2016), *Material info for PI-ETPU 95-250 Carbon Black*.
<http://rubber3dprinting.com/pi-etpu-95-250-carbon-black/>
- [21] Palmiga Innovation (2016), *PI-ETPU 95-250 Carbon Black*.
http://rubber3dprinting.com/PI-ETPU_95-250_Carbon_Black_TDSheet_20160609.pdf
- [22] Qi, H. and M. Boyce (2005), Stress-strain behavior of thermoplastic polyurethanes, **vol. 37**, no.8, pp. 817 – 839, ISSN 0167-6636,
doi:<http://dx.doi.org/10.1016/j.mechmat.2004.08.001>.
<http://www.sciencedirect.com/science/article/pii/S0167663604001140>
- [23] R.M. Crowder (1998), Tactile sensing.
<http://www.southampton.ac.uk/~rmc1/robotics/artactile.htm>
- [24] da Silva, J. G., A. A. de Carvalho and D. D. da Silva (2002), A strain gauge tactile sensor for finger-mounted applications, **vol. 51**, no.1, pp. 18–22, ISSN 0018-9456,
doi:10.1109/19.989890.
- [The Engineering ToolBox] The Engineering ToolBox (), Modulus of Elasticity or Young's Modulus - and Tensile Modulus for common Materials.
http://www.engineeringtoolbox.com/young-modulus-d_417.html
- [26] Tiwana, M. I., S. J. Redmond and N. H. Lovell (2012), A review of tactile sensing technologies with applications in biomedical engineering, *Sensors and Actuators A: Physical*, **vol. 179**, pp. 17 – 31, ISSN 0924-4247,
doi:<http://dx.doi.org/10.1016/j.sna.2012.02.051>.
<http://www.sciencedirect.com/science/article/pii/S0924424712001641>
- [27] Tsukinovsky, D., Zaretsky, E. and Rutkevich, I. (1997), Material Behavior in Plane Polyurethane-Polyurethane Impact with Velocities from 10 to 400 m/sec, **vol. 07**, no.C3, pp. C3–335–C3–339, doi:10.1051/jp4:1997359.
<https://doi.org/10.1051/jp4:1997359>
- [28] Vatani, M., E. D. Engeberg and J.-W. Choi (2015), Conformal direct-print of piezoresistive polymer/nanocomposites for compliant multi-layer tactile sensors, *Additive Manufacturing*, **vol. 7**, pp. 73 – 82, ISSN 2214-8604,

- doi:<http://dx.doi.org/10.1016/j.addma.2014.12.009>.
<http://www.sciencedirect.com/science/article/pii/S2214860414000335>
- [29] Vishay Precision Group (2014), *Single-Point Aluminum Load Cell*.
<http://www.vishaypg.com/docs/12007/1022.pdf>
- [30] Wei, Y. and Q. Xu (2015), An overview of micro-force sensing techniques, *Sensors and Actuators A: Physical*, **vol. 234**, pp. 359 – 374, ISSN 0924-4247,
doi:<http://dx.doi.org/10.1016/j.sna.2015.09.028>.
<http://www.sciencedirect.com/science/article/pii/S092442471530145X>

Acknowledgements

I would like to express my gratitude towards a couple of people who have helped me during my research. I would like to thank Gijs Krijnen for his advice and support throughout the research, Remco Sanders for his help with preparing the measurement setups, Martijn Schouten for sharing his force calibration curve of the SMAC actuator and his MATLAB script to digitally log data of the SMU and Gerjan Wolterink for suggesting some useful literature. Furthermore, I would like to thank all NIFTy members for their time and tips during the meetings and in general.